

Integration of spatial and single-cell data across modalities with weak linkage

Shuxiao Chen^{1,*}, Bokai Zhu^{2,3,*}, Sijia Huang¹, John W. Hickey³, Kevin Z. Lin¹, Michael Snyder⁴, William J. Greenleaf⁴, Garry P. Nolan^{2,3,†}, Nancy R. Zhang^{1,†}, and Zongming Ma^{1,†}

¹Department of Statistics and Data Science, The Wharton School, University of Pennsylvania, PA, United States

²Department of Microbiology and Immunology, Stanford University, Stanford, CA, United States

³Department of Pathology, Stanford University, Stanford, CA, United States

⁴Department of Genetics, Stanford University, Stanford, CA, United States

[†]Senior Authors

*Equal Contributions

Abstract: single-cell sequencing methods have enabled the profiling of multiple types of molecular readouts at cellular resolution, and recent developments in spatial barcoding, in situ hybridization, and in situ sequencing allow such molecular readouts to retain their spatial context. Since no technology can provide complete characterization across all layers of biological modalities within the same cell, there is pervasive need for computational cross-modal integration (also called diagonal integration) of single-cell and spatial omics data. For current methods, the feasibility of cross-modal integration relies on the existence of highly correlated, a priori “linked” features. When such linked features are few or uninformative, a scenario that we call “weak linkage”, existing methods fail. We developed MaxFuse, a cross-modal data integration method that, through iterative co-embedding, data smoothing, and cell matching, leverages all information in each modality to obtain high-quality integration. MaxFuse is modality-agnostic and, through comprehensive benchmarks on single-cell and spatial ground-truth multi-ome datasets, demonstrates high robustness and accuracy in the weak linkage scenario. A prototypical example of weak linkage is the integration of spatial proteomic data with single-cell sequencing data. On two example analyses of this type, we demonstrate how MaxFuse enables the spatial consolidation of proteomic, transcriptomic and epigenomic information at single-cell resolution on the same tissue section.

Single cell | Multi-modal integration | Diagonal integration | Matching | Multi-omics | Spatial-omics | Protein | RNA | ATAC

Correspondence: gnolan@stanford.edu, nzh@wharton.upenn.edu, zongming@wharton.upenn.edu

Introduction

Recent technological advances have enabled the profiling of multiple biological modalities within individual cells, over many cells in parallel. The growing list of modalities that can now be profiled at the single-cell level include proteome and metabolome (1, 2), transcriptome (3), and various aspects of the epigenome such as methylation (4), histone modification (5–7), and chromatin accessibility (5, 8). In addition to technologies that operate on dissociated single cells, rapid progress has been made on the in situ measurement of transcriptome (9), proteome (10–14), epigenome (15), and other modalities on histological tissue sections at single-cell or close to single-cell resolution, retaining the spatial context. These advances have spawned consortia-level efforts to con-

struct multiomic single-cell and spatial atlases of each and every organ, across species, in healthy and diseased states.

To harness the new technologies and growing data resources for biological discovery, a primary challenge is the reliable integration of data across modalities. Cross-modal integration, also referred to as “diagonal integration” (16, 17), is the alignment of single cells or spatial spots across datasets where different features (or modalities) are profiled in each dataset. An example is the alignment of cells in a CODEX dataset, which measures protein abundance, to cells in a single-cell RNA sequencing (scRNA-seq) dataset, which measures RNA expression. This cross-modal integration step underpins many types of downstream analyses, and its importance is evident in the myriad methods that have already been developed to tackle it (18–24).

Despite the progress in this area, key limitations still hinder reliable cross-modal integration, as highlighted by recent surveys (16, 17, 25). A key factor limiting the accuracy of existing methods is the strength of *linkage* between modalities, as we define below. A feature is “linked” between two modalities if it can be measured in, or predicted by, both modalities. In the terminology of (16, 17), these linked features can serve as “anchors” for the integration. For example, to integrate single-cell or spatial ATAC sequencing (ATAC-seq) and single-cell or spatial RNA-seq data, most existing methods predict the “activity” for each gene in each cell/spot of the ATAC-seq data based on the accessibility of the gene’s surrounding chromatin; then, each gene’s ATAC activity can be linked to its RNA expression, mapping cells from the two datasets into the same feature space. Similarly, between RNA and protein assays, the abundance of each protein in the protein assay can be linked to the expression of its coding gene in the RNA assay. With the exception of bindSC (26), all existing methods, to our knowledge, rely crucially on the linked features and are designed for scenarios where there is a large number of linked features that exhibit strong cross-modality correlation, a situation that we refer to as “strong linkage”. For example, between scRNA-seq and scATAC-seq, every gene in the genome can be linked, and the correlation between gene activity and RNA expression is often high enough for enough genes to allow for precise integration (18, 19, 22). To achieve strong linkage, some methods attempt to learn a mapping from the features of one modality to the features of

87 the other modality through a “training set” consisting of data 144
88 where both modalities are simultaneously observed in each 145
89 cell/spot (23, 27). While this strategy may be applicable to- 146
90 wards the integration of data from biological systems that are 147
91 similar to the training set, it is questionable how well it can 148
92 generalize to unseen systems. 149

93 Cross-modality integration in scenarios of weak linkage, 150
94 where the number of linked features is small and/or the 151
95 between-modality correlation for the linked features is weak, 152
96 is especially challenging. A prototypical example of weak 153
97 linkage is between targeted protein assays (14, 28) and 154
98 transcriptome/epigenome assays such as scRNA-seq and 155
99 scATAC-seq. Such scenarios are becoming extremely com- 156
100 mon as spatial proteomic technologies are receiving wide- 157
101 spread adoption (10–14), complementing RNA and ATAC se- 158
102 quencing in achieving more complete tissue characterization 159
103 (see, for example, (29–32)). We will reveal, through compre- 160
104 hensive benchmarks, the limitations of existing state-of-the- 161
105 art methods in such difficult cases.

106 Under both strong and weak linkage, the evaluation of ex- 162
107 isting methods have leaned heavily on systems with highly 163
108 distinct cell types whose separation only requires a crude 164
109 feature-level mapping between modalities. In fact, most ex- 165
110 isting methods explicitly focus on the goal of “label transfer”, 166
111 that is, the transfer of cell type labels from one modality to the 167
112 other. This goal only requires the integration to be accurate at 168
113 the resolution of the label. As we demonstrate in our bench- 169
114 marks, even this seemingly modest goal of label transfer for 170
115 major cell types is unattainable in weak linkage scenarios by 171
116 current methods, much less the more challenging goal of in- 172
117 tegration in continuously transitioning cell populations where 173
118 subtle distinctions need to be preserved between closely re- 174
119 lated states. Yet, key biological discoveries often hinge on 175
120 the accurate preservation of fine cell state distinctions during 176
121 integration, 177

122 To address the above limitations, we developed MaxFuse 178
123 (MAtching X-modality via FUZZY Smoothed Embedding), a 179
124 model free, highly adaptive method that can accurately inte- 180
125 grate data across weakly linked modalities. MaxFuse goes 181
126 beyond label transfer and attempts to match cells to pre- 182
127 cise positions on a graph-smoothed low-dimensional embed- 183
128 ding. MaxFuse starts by denoising the linked features in each 184
129 modality through borrowing information from all of the fea- 185
130 tures, and then performs an initial crude matching of cells 186
131 based on the denoised linked features. Then, MaxFuse iter- 187
132 atively refines the matching step based on graph smoothing, 188
133 linear assignment, and CCA. These iterations use informa- 189
134 tion from all features in both modalities to improve upon the 190
135 initial matching. The initial feature linkage may be derived 191
136 from domain knowledge or an existing integration, and thus, 192
137 MaxFuse can also be used to improve upon any existing inte- 193
138 gration methods. 194

139 We systematically benchmarked the performance of Max- 195
140 Fuse across protein, RNA, and chromatin accessibility 196
141 single-cell multiome ground-truth datasets. Across a wide 197
142 variety of datasets, MaxFuse has superior performance com- 198
143 pared to other state-of-the-art integration methods. Although 199

the largest improvements in accuracy are observed under weak linkage, under strong linkage MaxFuse is comparable to the current best method in integration performance with substantial improvement in speed.

We further demonstrate the analyses enabled by MaxFuse with two examples. First, in the integration of scRNA-seq and CODEX multiplexed in situ protein profiling data from the human tonsil, we show that MaxFuse can recover correct spatial gradients in the RNA expression of genes not included in the 46-marker protein panel. Next, MaxFuse is applied to an atlas-level integration of spatial proteomic and single-cell sequencing datasets, as part of a consortium-level effort to map cell organization and function across different regions of the human intestine (32). We demonstrate how to perform tri-modal integration of CODEX, snRNA-seq, and snATAC-seq data to recover spatial patterns of RNA expression and transcription factor binding site accessibility at single-cell resolution.

Results

Cross-modality matching of single cells via iterative fuzzy smoothed embedding. Let data from the two modalities be represented by a pair of cell-by-feature matrices that contain all measured features in each modality. For convenience, call the two modalities Y and Z . In addition, we represent the initial knowledge about the linkage between the two modalities as another pair of cell-by-feature matrices whose columns have one-to-one correspondences. To distinguish between these two pairs of matrices, we call the former all-feature matrices and the latter linked-feature matrices. For example, when one modality is protein abundance over a small antibody panel and the other is RNA expression over the whole transcriptome, the two all-feature matrices have drastically different numbers of columns, one being the number of proteins in the panel and the other being the number of genes in the transcriptome; the linked feature matrices, on the other hand, have equal number of columns, where each column in the protein matrix is one protein and its corresponding column in the RNA linked-feature matrix is the gene that codes for the protein. When the number of cells is large, we recommend aggregating cells with similar features into meta-cells, as described in Materials & Methods, prior to applying MaxFuse. In that case, each row in the above matrices would represent a meta-cell. The procedure below does not depend on whether single- or meta-cells are used, and thus we will refer to each row as a “cell”. The two pairs of matrices form the input of the MaxFuse pipeline in Figure 1A.

Stage 1 of MaxFuse aims to summarize cell-cell similarity within each modality and learn an initial cross-modal matching of cells. As shown in Figure 1A, this stage consists of three major steps. In step 1, for each modality, we use all features to compute a fuzzy nearest-neighbor graph connecting all cells measured in that modality. This graph, by utilizing the information in all features, provides the best possible summary of the cell-cell similarity for the given modality. In particular, cells that are close in this graph should

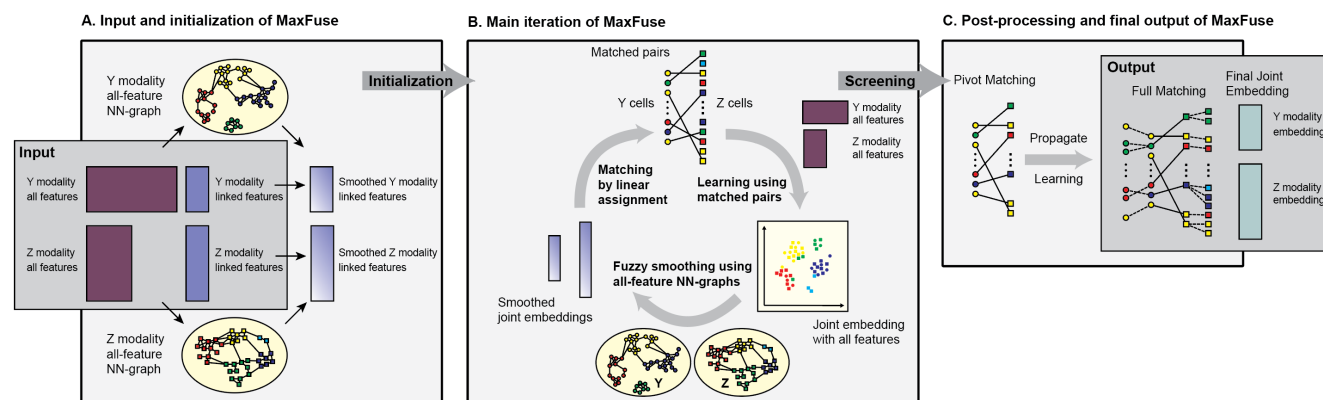


Figure 1: Overview of MaxFuse pipeline. (A) The input consists of two pairs of matrices. The first pair consists of all features from each modality, and the second pair consists of only the linked features. MaxFuse uses all features within each modality to create a nearest-neighbor graph (all-feature NN-graph) for cells in that modality. Fuzzy smoothing induced by the all-feature NN-graph is applied to the linked features in each modality. Cross-modal cell matching based on the smoothed linked features initializes the iterations in (B). (B) In each iteration, MaxFuse starts with a list of matched cell pairs. A cross-modal cell pair is called a pivot. MaxFuse learns CCA loadings over all features from both modalities based on these pivots. These CCA loadings allow the computation of CCA scores for each cell (including cells not in any pivot), which are used to obtain a joint embedding of all cells across both modalities. For each modality, the embedding coordinates then undergo fuzzy smoothing based on the modality-specific all-feature NN-graphs (obtained in (A)). The smoothed embedding coordinates are supplied to a linear assignment algorithm which produces an updated list of matched pairs to start the next iteration. (C) After iterations end, MaxFuse screens the final list of pivots to remove low-quality matches. The retained pairs are called refined pivots. Within each modality, any cell that is not part of a refined pivot is connected to its nearest neighbor that belongs to a refined pivot and is matched to the cell from the other modality in this pivot. This propagation step results in a full matching. MaxFuse further learns the final CCA loadings over all features from both modalities based on the refined pivots. The resulting CCA scores give the final joint embedding coordinates.

200 have comparable values for their linked features. Thus, in 232
 201 step 2 of stage 1, MaxFuse boosts the signal-to-noise ratio in 233
 202 the linked features within each modality by shrinking their 234
 203 values, for each cell, towards the cell's graph-neighborhood 235
 204 average. We call this step "fuzzy smoothing". After fuzzy 236
 205 smoothing of linked features within each modality, MaxFuse 237
 206 computes in step 3 distances between all cross-modal cell 238
 207 pairs based on the smoothed linked features and applies linear 239
 208 assignment (33) on the cross-modal pairwise distances to ob- 240
 209 tain an initial matching of cells. The initial matching serves 241
 210 as the starting point of stage 2 of MaxFuse. 242

211 Stage 2 of MaxFuse, shown in Figure 1B, aims at improving 243
 212 cross-modal cell matching quality by iterating the sequence 244
 213 of joint embedding, fuzzy smoothing, and linear assignment 245
 214 steps. Starting with the initial matches obtained in stage 1, in 246
 215 each iteration, MaxFuse first learns a linear *joint embedding* 247
 216 of cells across modalities by computing a canonical correla- 248
 217 tion based on all features of the cross-modal matched cell 249
 218 pairs. Then, coordinates of this joint embedding are treated 250
 219 as new linked features of each modality and *fuzzy smoothing* 251
 220 is applied on them based on the all-feature nearest-neighbor 252
 221 graphs computed in stage 1. Finally, MaxFuse updates the 253
 222 cell-matching across modalities by applying *linear assign-* 254
 223 *ment* on the pairwise distances of these fuzzy-smoothed joint 255
 224 embedding coordinates. The resulting matching then starts 256
 225 the next iterate. Matching quality improves with each iter- 257
 226 ation until available information in all features, and not just 258
 227 the linked features, have been used. 259

228 Stage 3 of MaxFuse aims at post-processing the last cross- 260
 229 modal cell matching from stage 2 and producing final out- 261
 230 puts. First, MaxFuse screens the matched pairs from the last 262
 231 iterate in stage 2, retaining high quality matches as pivots. 263

The pivots are used in two complementary ways: (i) they are
 used one last time to compute a final joint embedding of all
 cells in both modalities; (ii) for any unmatched cell in either
 modality, its closest neighbor within the same modality that
 belongs to a pivot is identified and, as long as its distance to
 this neighbor is below a threshold, the match in the pivot is
 propagated to the cell. Thus, the final output of MaxFuse has
 two components: (i) a list of matched pairs across modalities,
 and (ii) a joint embedding of all cells in both modalities.
 More details on the MaxFuse algorithm are given in Materials
 & Methods.

**Integration of transcriptome and targeted protein data
 with varying protein panel sizes.** We benchmarked Max-
 Fuse on a CITE-seq dataset (34) containing simultaneous
 measurements of 228 protein markers and whole transcrip-
 tome on peripheral blood mononuclear cells. For compari-
 son, we also applied four state-of-the-art integration meth-
 ods: Seurat (V3) (24), Liger (22), Harmony (20), and BindSC
 (26) to this same dataset. Protein names were converted to
 RNA names manually to link the features between datasets.
 In each repetition of our experiment, we randomly subsam-
 pled 10,000 cells, applied all methods, and assessed using the
 benchmarking criteria to be described below. We performed
 5 such repetitions and averaged the criteria across repetitions.
 We masked the known cell-cell matching between the pro-
 tein and RNA modalities when applying all methods (treating
 Protein and RNA as two unpaired modalities), and then used
 the known matching for assessment.

Methods are assessed using six different criteria that mea-
 sure both cell-type-level label transfer accuracy as well as
 cell-level matching accuracy. The first two criteria are based
 on label transfer accuracy. Cells are annotated at two levels

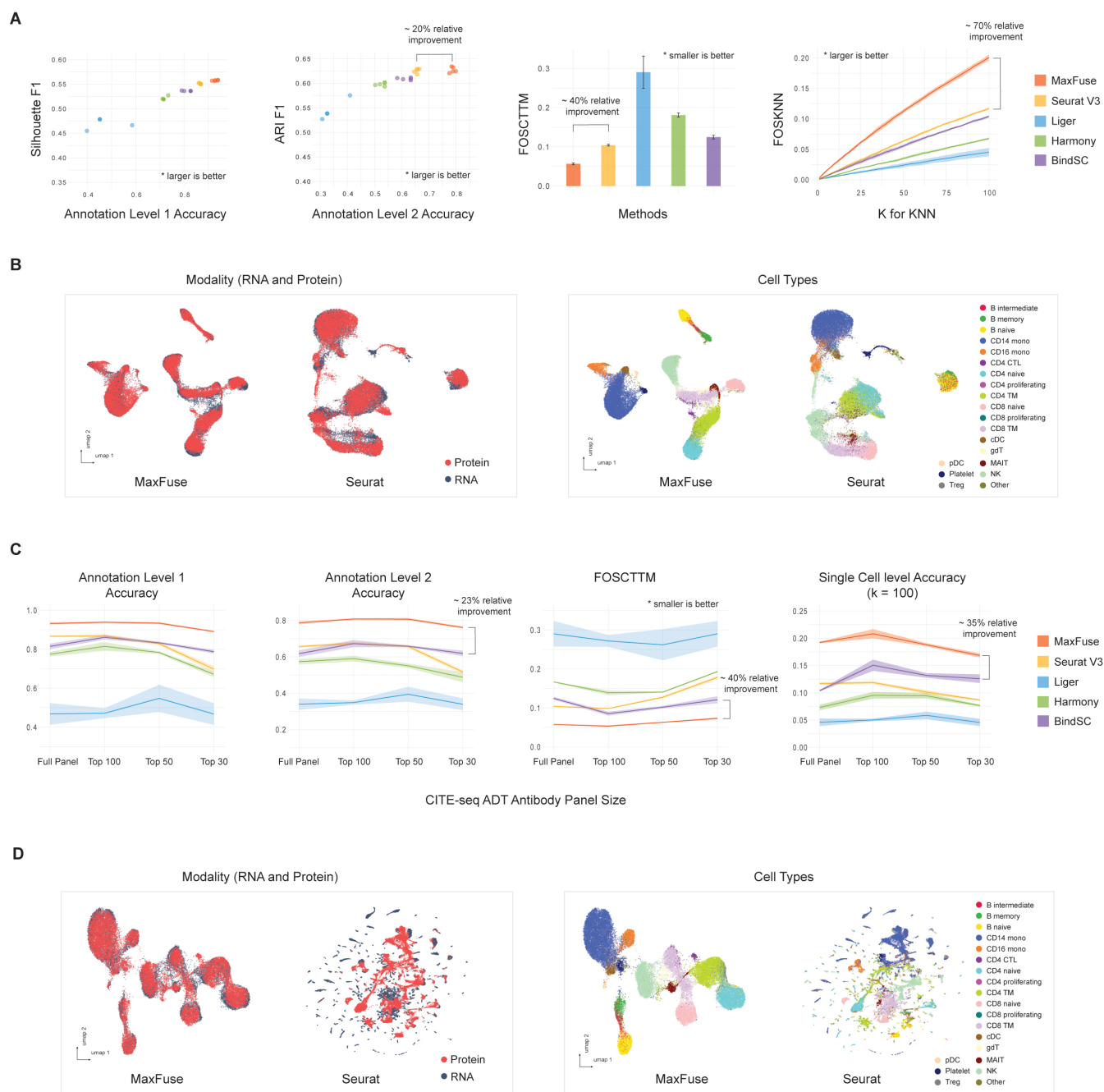


Figure 2: Benchmark on ground-truth CITE-seq PBMC data with full and reduced antibody panels. (A) Matching and integration performance of MaxFuse and other methods on CITE-seq PBMC dataset with full antibody panel (228 antibodies). **(B)** UMAP visualization of MaxFuse and Seurat (V3) integration results of CITE-seq PBMC with full panel, colored by modality (left) or cell type (right). **(C)** Matching and integration performance of MaxFuse and other methods on CITE-seq PBMC dataset with reduced antibody panels. **(D)** UMAP visualization of MaxFuse and Seurat (V3) integration results of CITE-seq PBMC with the 30 most informative of the original 228 antibodies, colored by modality (left) or cell type (right).

264 of granularity: level-1, which differentiates between 8 ma- 274
 265 jor cell types, and level-2, a finer classification which dif- 275
 266 ferentiates between 20 cell types. Label transfer accuracy is 276
 267 expected to be higher for level-1 labels than for level-2 la- 277
 268 bels. The proportion of matched pairs that share the same 278
 269 label at both annotation levels are reported, with higher pro- 279
 270 portions indicating higher matching quality. The next two 280
 271 criteria measure the quality of the cross-modal joint embed- 281
 272 ding of cells. A high-quality joint embedding should preserve 282
 273 biological signal, as reflected by the separation of known cell 283

types, while mixing the two modalities as uniformly as possible. Usually, there is a trade-off between biological signal preservation and uniformity of mixing. Thus, we report the F_1 scores computed based on average silhouette width (slt_f1) and adjusted Rand index (ari_f1), as proposed in Tran et al. (35). These scores aggregate quality assessments of biological signal preservation and modality mixing. For both criteria, higher F_1 indicates a better embedding. The fifth criterion is FOSCTTM, Fraction Of Samples Closer Than True Match (19, 36, 37), that quantifies the quality of joint embed-

ding at single-cell resolution. For each cell, one can compute the fraction of cells in the other modality that is closer than its true match in the joint embedding. FOSCTTM is the average of this fraction over all cells in both modalities. The lower this measure, the closer the true matches are in the joint embedding, and hence, the better the joint embedding. The last criterion is FOSKNN, Fraction Of Samples whose true matches are among their K-Nearest Neighbors in the joint embedding space. For any given $k \geq 1$, the higher this proportion, the better the joint embedding. For precise definitions and details of these criteria, see Materials & Methods. Among all criteria described above, MaxFuse uniformly dominates the methods by a sizable margin (Figure 2A). Importantly, MaxFuse provides accurate cell matching across weakly-linked modalities (level 1 accuracy 93.9%, + ~ 7% to the second best method, Figure S2B). The UMAP plots calculated based on the post-integration embedding from respective methods are shown in Figure 2B, colored by modality and by cell type. MaxFuse achieves both better mixing of the two modalities (left panel) and better preservation of biological signals (right panel). For example, B cell subtypes (B naive, intermediate, and memory cells) present a nicely resolved developmental trajectory after MaxFuse integration, but not after integration by other methods. It is common to have an antibody panel that is of significantly smaller size than 228, especially for the emerging spatial-proteomic datasets. To benchmark the performance of MaxFuse against existing methods for smaller antibody panels, we ordered the proteins according to their importance for differentiating cell types (See Materials & Methods for details). We repeated the foregoing experiments when only the top 100, 50, and 30 most important proteins are used in the matching and integration process. At each antibody panel size, we ran the experiment over five independent repetitions with randomly subsampled 10,000 cells, and average the cell type annotation level matching accuracy, FOSCTTM and FOSKNN across repetitions (Figure 2C). Regardless of panel change, MaxFuse consistently outperformed other methods. Additionally, MaxFuse successfully mitigated the effect of reduced panel size on integration quality: Even when the antibody panel size was reduced to 30, MaxFuse maintained a > 90% annotation level 1 accuracy while other methods produced variable and low quality cell matching results (~ 10 – 70%, Figure S2B). Similarly, with a reduced antibody panel size (eg. 30 antibodies), the integrated UMAP embedding (38) produced by other methods blurs the distinction between cell types, while MaxFuse embedding still accurately captures the subtle structure of highly granular cell subtypes (e.g., the B cell subpopulations, Figure 2D and Figure S2A).

Systematic benchmark across multiple ground-truth multiome modalities. We further benchmarked MaxFuse on four additional single-cell multiome datasets. The first is a CITE-seq dataset of human bone marrow mononuclear cells (BMMCs) that provides cell-matched measurements of the full transcriptome along with an antibody panel of size 25 (34). The second is an ABseq dataset, also of BMMCs,

with an antibody panel of size 97 and the whole transcriptome (39). The third is an ASAP-seq PBMC dataset (40) with 227 antibodies and the whole epigenome measured in ATAC fragments. The fourth is a TEA-seq PBMC dataset (41) where we focused on the simultaneous measurements of 46 antibodies and the whole epigenome measured in ATAC fragments. Together, these datasets represent a diverse collection of measurement technologies over different modality pairs. We benchmarked the performance of MaxFuse against Seurat (V3), Liger, Harmony, and BindSC on these datasets. For datasets with simultaneous RNA and protein features, we linked each protein to its coding gene. For datasets with simultaneous ATAC and protein measurements, we linked each protein to the gene activity score (42) computed from the ATAC fragments mapping near its coding gene. As in the previous case, the known cell-cell correspondence across modalities were masked in the matching and integration stage for all methods, but used afterwards for evaluation.

We compared the performances of MaxFuse and the other four methods on these datasets using the collection of matching and integration quality measures described in the previous section (Figure 3A): cell type annotation matching accuracy, FOSCTTM, FOSKNN (K set as 1/200 dataset size), Silhouette F1 score, and ARI F1. Overall, MaxFuse outperformed other methods, often by a sizable margin (eg. ~ 20% relative improvement in terms of the metrics measured, Figure 3A and Figure S3.1A).

UMAPs of the MaxFuse cross-modal joint embeddings for each dataset are shown in Figure 3B, with the top row colored by modality and the bottom row colored by cell type annotation. Across the integration scenarios, MaxFuse mixed different modalities well in joint embeddings while retaining separation between cell types. Compared to the UMAPs of joint embeddings produced by other methods, MaxFuse consistently achieves substantial improvements (Figure 3B and Figure S3.2 A).

As a counterpoint to the above integration scenarios, we also considered the problem of integration of scRNA-seq and scATAC-seq data, on which multiple methods have demonstrated feasibility (18, 19, 22). The degree of overlap in the information contained in the RNA and ATAC modalities has been systematically measured in Lin and Zhang (43), where it was shown that, in terms of cell population structure, the information shared across RNA and ATAC is much higher than the information shared between RNA and protein for commonly used targeted protein panels. Thus, RNA and ATAC has stronger linkage and should be easier to integrate. We benchmarked MaxFuse against state-of-the-art methods for this problem on four public multiome datasets that simultaneously measure the chromatin accessibility and transcriptome expression for each cell: 10x mononuclear cells from peripheral blood (44), cells from embryonic mouse brain at day 18 postconception (44), cells from developing human cerebral cortex (45), and cells from human retina (46). The integration quality criteria described in the previous subsection are used to assess all methods, shown in Supplementary Materials. Across datasets and evaluation metrics, MaxFuse

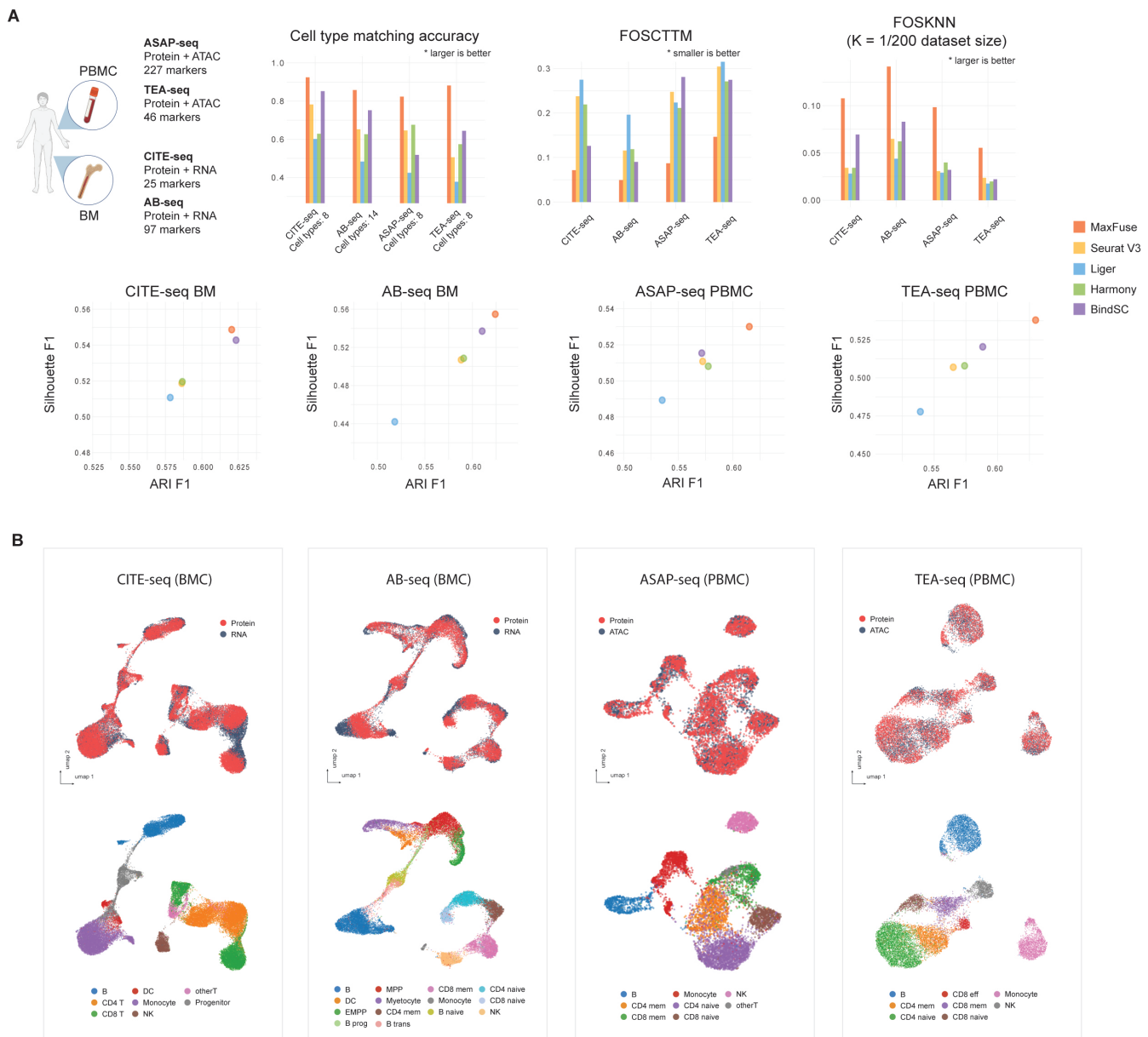


Figure 3: Systematic benchmark across multiple ground-truth data types with MaxFuse (A) Four different multiome datasets, generated by different technologies, were benchmarked. Cell type matching accuracy, FOSCTTM, FOSKNN (with $K = 0.5\%$ total cell counts of each dataset), and ARI and Silhouette F1 were evaluated across 5 methods. **(B)** UMAP visualization of MaxFuse integration results for the four ground-truth multiome datasets.

398 achieves best or close-to-best performance among methods, 413
 399 and is comparable to scGLUE. However, MaxFuse is much 414
 400 faster than scGLUE. For example, for the integration of a 415
 401 dataset of 20,000 cells, MaxFuse took <5 minutes to finish 416
 402 on a laptop with M1 Max chip while scGLUE took hours on 417
 403 a comparable platform without CUDA acceleration. 418

404 **Cross-modal integration of scRNA-seq and spatial** 420
 405 **proteomic data enables information-rich spatial pat-** 421
 406 **tern discovery.** MaxFuse is particularly motivated by scen- 422
 407 arios where the signal-to-noise ratio in the cross-modal 423
 408 linked features is low. Weak linkage is especially common
 409 in spatial-omic data types due to technical limitations. For 424
 410 example, high resolution spatial proteomic methods such as 425
 411 CODEX, MIBI-TOF, IMC, and CosMx SMI can profile, at 426
 412 sub-cellular resolution, a panel of 30-100 proteins (10–13). 427

Integration of such spatial proteomics datasets with single-
 cell transcriptomic and epigenomic datasets of the same tis-
 sue is often of interest, and particularly challenging due to
 the small number of markers in the spatial dataset and the
 weak linkage between modalities that is caused by both bio-
 logical and technical differences. Thus, we demonstrated
 and benchmarked MaxFuse on the integration of CODEX multi-
 plex imaging with 46 markers (47) with single-cell RNA-seq
 (48) of human tonsils from two separate studies (Figure 4A).
 Figure 4B shows the UMAPs of the MaxFuse integration col-
 ored by modality and by 6 major cell types.

Based on the pre-described benchmarking metrics, MaxFuse
 is the only method capable of integrating spatial proteomic
 and single-cell RNA-seq data. Existing state-of-the-art meth-
 ods, Seurat (V3), Liger, Bindsc, and Harmony, failed to pro-

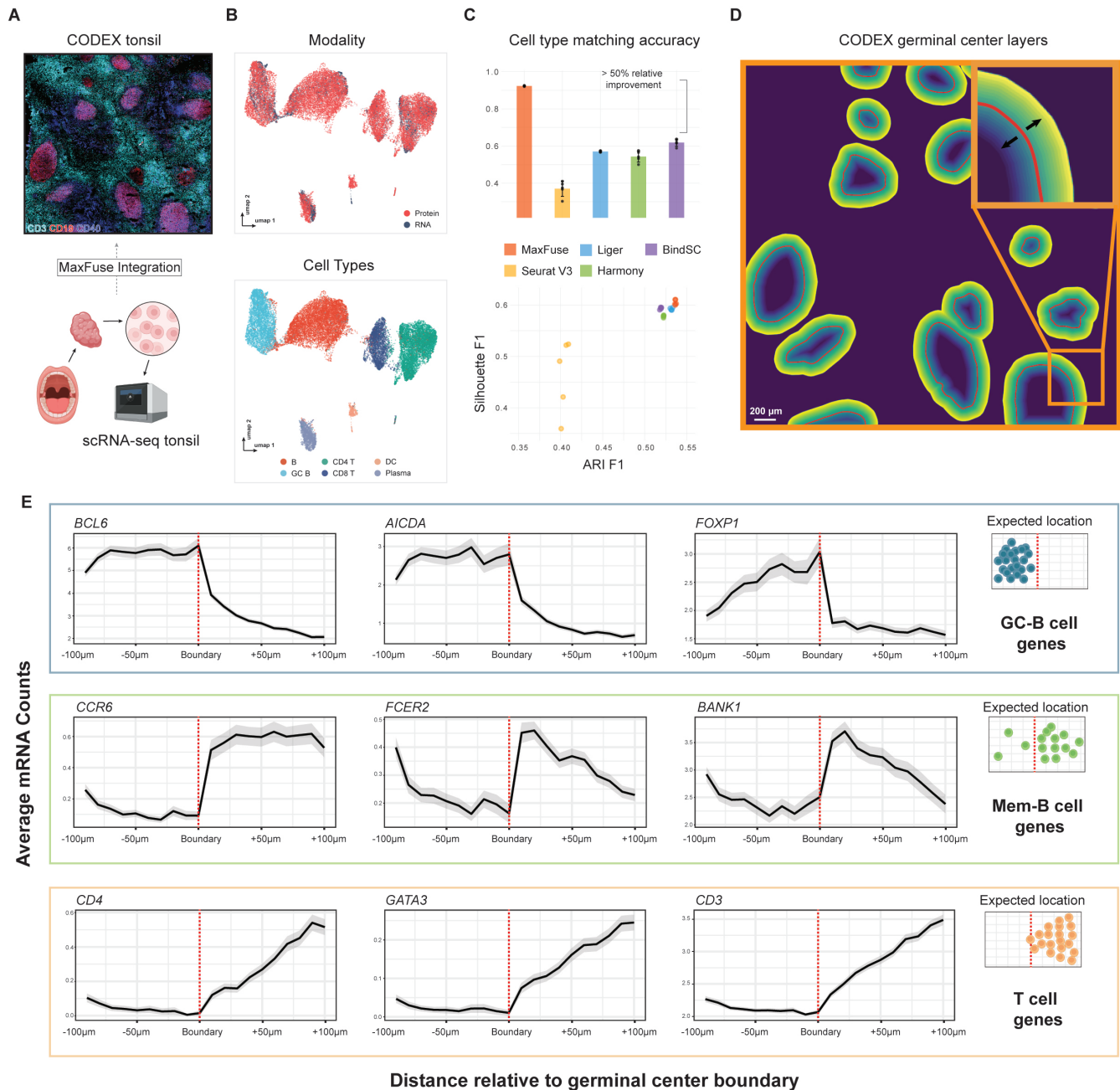


Figure 4: MaxFuse enables information-rich spatial pattern discovery (A) MaxFuse integrates human tonsil single-cell data: one dataset by CODEX from Kennedy-Darling et al (47) (upper panel), the other dataset by scRNA-seq from King et al (48) (lower panel). (B) UMAP visualization of MaxFuse integration of tonsil CODEX and scRNA-seq data, colored by modality (upper panel) and cell type (lower panel). (C) Metrics (cell type matching accuracy, Silhouette F1 and ARI F1 score) evaluating performance of MaxFuse and other methods. Five batches of randomly sampled CODEX and scRNA-seq cells (total of 40k each batch) were sampled, and used for benchmarking for all methods. (D) Illustration of cell layers extending inwards/outwards from the germinal center boundary, with each layer consisting of 30 pixels ($\sim 11\mu\text{m}$). A total of 10 layers extending in each direction were examined. (E) For each of 9 genes, the average mRNA counts (linked by MaxFuse) across cells in each layer are plotted versus the position of the layer in reference to the germinal center boundary (inward on the left of boundary, outward on the right). For each group of 3 genes (row), their expected expression profile in reference to the germinal center boundary is shown on the right.

duce an embedding that integrates the two modalities while preserving the cell population structure (Figure 4B and Figure S4.1A). Evaluation results based on cell-type matching accuracy is consistent with evaluation results based on the joint embedding. At the level of the 6 major cell types shown in Figure 4B, MaxFuse is able to achieve high label transfer accuracy (93.3%), while the other methods fail to preserve cell type distinctions (40% - 60%, Figure 4B and Figure S4.1B). We further assessed whether MaxFuse can preserve, during integration, the more subtle spatial variations within a cell type that are captured by CODEX. We manually delineated the boundaries of each individual germinal center (GC) from the CODEX tonsil images based on CD19, CD21, Ki-67 protein expression patterns. From the boundaries, we then extended outward or inward, with each step covering roughly one layer of cells (one step = 30 pixels erosion/dilation) (Figure 4C). Then, for each layer of cells, we calculated the average counts of specific genes, based on the scRNA-seq cells that match to CODEX cells of that layer. We then asked if known position-specific gene expression patterns relative to the germinal center boundary are recovered in the integrated scRNA-seq data. Indeed, MaxFuse was able to reconstruct the spatial pattern of the GC from disassociated transcriptomic data (Figure 4D): For GC-specific genes *BCL6*, *AICDA* and *FOXP1* (49–51) that relate to germinal center functionality, we observed high expression within the boundary and a sharp drop in expression after passing the boundary layer; for genes related to B cell memory *CCR6*, *BANK1* and *FCER2* (51–53) that should be enriched in B cells exiting from the GC, we indeed saw a gradual increase outside of the GC and then a quick decrease as the layer fully expands into the T cell region; and finally for T cell related genes, for example *CD4*, *GATA3* and *CD3* (54), we indeed saw a rapid increase outside of the GC boundary but no expression within. In comparison, the integration with scRNA-seq produced by other methods was incapable of accurately reconstructing the GC spatial pattern (Figure S4.2A).

Tri-modal atlas-level integration of spatial and single-cell data with MaxFuse. In the consortium-level effort to generate a comprehensive atlas across different regions of the human intestine, colon and small bowel tissue from healthy human donors were collected and systematically profiled by CODEX, snRNA-seq, and snATAC-seq (32). We applied MaxFuse to the integration of these three modalities (Figure 5A), with the goal of constructing high-resolution spatial maps of full transcriptome RNA expression and transcription factor binding accessibility. To perform tri-omic integration, we first conducted pairwise alignment of cells between protein (CODEX) and RNA (snRNA-seq), and cells between RNA (snRNA-seq) and ATAC (snATAC-seq), as previously described. The two sets of bi-modal cell-pairing pivots were then “chained” together, with the pivot cells in the RNA modality serving as the intermediary. This “chaining” created a set of pivots linking all three modalities: Protein, RNA, and ATAC. Subsequently, we used these pivots to calculate a tri-omic embedding via generalized CCA (gcca) (50

(21, 55). This allows for a joint UMAP embedding of the three modalities, shown in Figure 5B. We see that distinctions between major cell types are preserved and modalities are mixed within each cell type.

The MaxFuse integration produces, effectively, a joint profile of protein abundance, RNA expression, and chromatin accessibility at single-cell spatial resolution on the same tissue section. To confirm the post-integration consistency between the three modalities, we inspected whether CODEX’s protein abundance aligns spatially with the expression and chromatin activity of the protein-coding gene, the spatial measurements of the latter two modalities imputed based on the MaxFuse integration. Figure 5C shows an example in CD163, a macrophage marker: The protein expression, RNA expression, and gene activity of CD163 are, as expected, uniquely enriched in the macrophage cell cluster (Figure 5C upper panel). Furthermore, protein, RNA, and ATAC activities of this gene all localize to the same spatial positions on the tissue section (Figure 5C lower panel). Other examples are shown in Supplementary Materials.

With the integration of the snATAC-seq and CODEX data, we can further map the spatial enrichment of transcription factor (TF) binding site accessibility. For each TF, this is achieved by first computing its motif enrichment score for each cell in the snATAC-seq data, and then the scores are transferred to the CODEX spatial positions based on the MaxFuse integration. Figure 5D shows such spatial profiles for 3 transcription factors: Binding motifs of *IRF4*, known to be a key regulator in immune cell differentiation (57), had increased accessibility in the immune-enriched compartments of the mucosa and submucosa layers (32). Binding motifs of *KLF4*, known to be required for the terminal differentiation of goblet cells (58), had heightened accessibility in the colonic crypts of the mucosa layer where goblet cells mature. Finally, binding motifs of *SRF*, a master regulator of smooth muscle gene expression, (59), had heightened accessibility in neighborhoods that are enriched for smooth muscle cells.

Discussion

In this paper, we conceptually separated cross-modal integration of single-cell data into two different scenarios: across modalities with strong linkage (e.g., ATAC-RNA integration) and across modalities with weak linkage (e.g., RNA-protein integration for a targeted protein panel). Most existing methods are developed for integration across strongly linked modalities, and our ground-truth benchmark results suggest that their performances decay significantly as the strength of cross-modal linkage weakens. MaxFuse is motivated by and focuses on the challenging case of weak linkage, which has become increasingly common as many emerging study designs include spatial data with targeted marker panels to be collected jointly with single-cell sequencing data. MaxFuse relies on two key ideas to overcome weak linkage: The first is a “fuzzy smoothing” procedure that denoises the linked features by moving their values towards their graph-smoothed values, with the graph determined by all features. The second is an iterative refinement procedure that improves

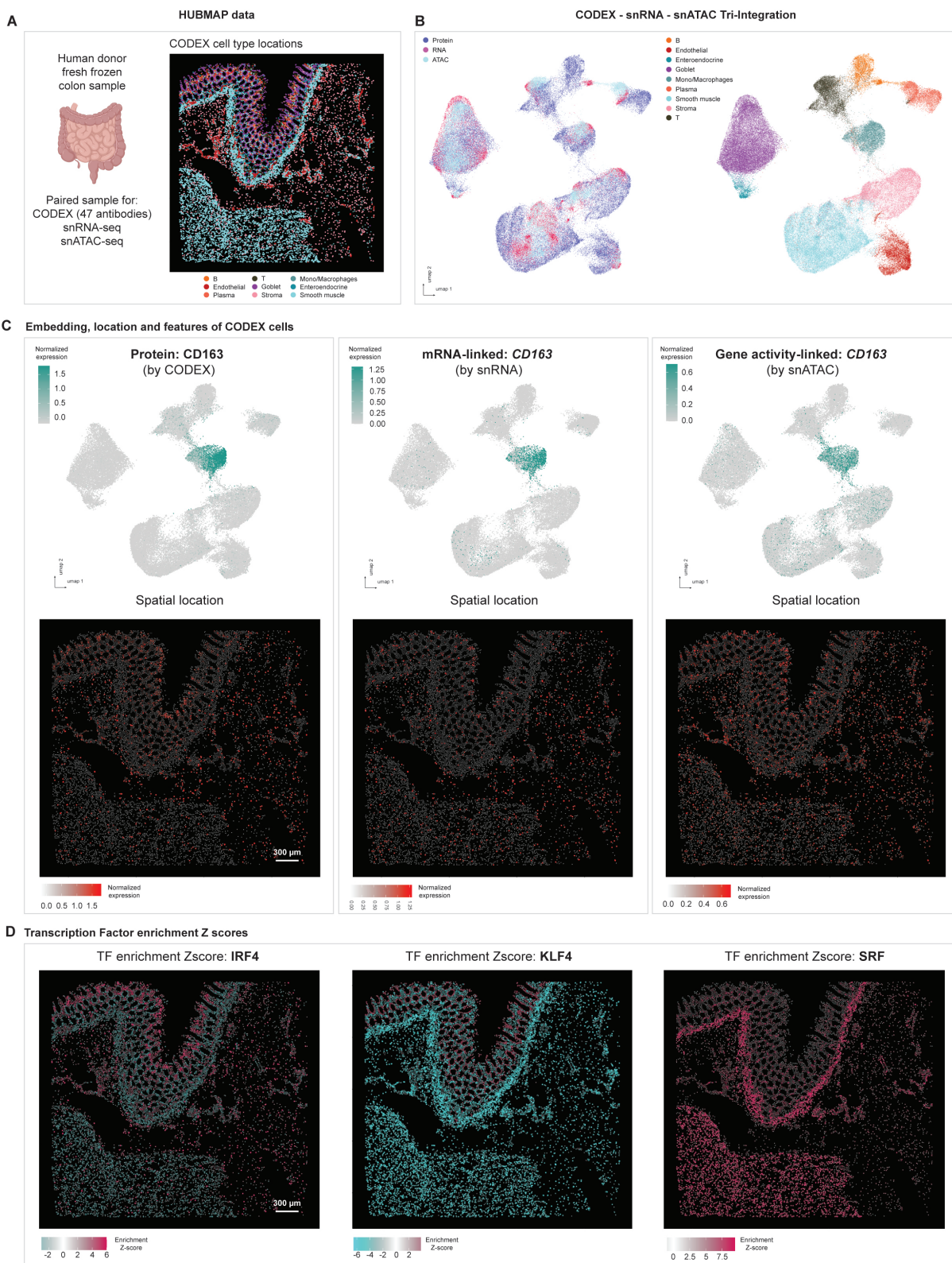


Figure 5: MaxFuse enables tri-modal integration with HUBMAP data (A) Overview of data: Patient paired CODEX, snRNA-seq, snATAC-seq single-cell human intestine data from HUBMAP consortium. Colon and small bowel data were integrated by MaxFuse respectively and this figure shows part of the colon data (CODEX data from one donor; snRNA-seq and snATAC-seq data from four donors). (B) UMAP visualization of the tri-modal integration embedding produced by MaxFuse, colored by modality: Protein, RNA and ATAC (left panel) and colored by cell type (right panel). (C) Upper panel: UMAP visualization of CODEX cells based on the integration embedding, overlaid with CD163 protein expression (from CODEX cells itself, left panel), *CD163* RNA expression (from matched snRNA-seq cells, middle panel), *CD163* gene activity score (from matched snATAC-seq cells). Lower panel: Spatial location of CODEX cells based on their centroids' x-y position, overlaid with the same expression features as in the upper panel. (D) Spatial location of CODEX cells based on their centroids' x-y position, overlaid with the transcription factor motif enrichment score (Z-score, calculated by chromVAR (56)), based on their matched snATAC-seq cells.

541 the cross-modal matching through an iterative cycle of co- 596
 542 embedding, graph-smoothing, and matching; this ensures 597
 543 that information from *all* features, in both modalities, are 598
 544 used to generate the final matching. We show that these key 599
 545 ideas allow MaxFuse to substantially improve upon state-of- 600
 546 the-art methods, achieving accurate integration of data from 601
 547 targeted protein assays with data from transcriptome- and 602
 548 epigenome-level assays. 603
 549 While MaxFuse is motivated by the weak linkage scenario, 604
 550 its applicability is universal. For strong linkage scenar- 605
 551 ios, methods based on deep learning, such as scGLUE, 606
 552 achieve state-of-the-art integration performance but is hin- 607
 553 dered by high computational costs. In comparison, MaxFuse 608
 554 achieves comparable performances as scGLUE on ground- 609
 555 truth strong-linkage benchmark datasets at a considerably 610
 556 lower computational cost. In addition, when joint embed- 611
 557 ding coordinates from other integration methods are avail- 612
 558 able, these coordinates could serve as linked features in Max- 613
 559 Fuse, which could then be further improved by the proced- 614
 560 ure. The light computation architecture and the flexibility 615
 561 in incorporating domain knowledge and existing integration 616
 562 results make the MaxFuse framework applicable to a wide 617
 563 range of cross-modal integration tasks.

564 Materials & Methods

565 The MaxFuse pipeline.

566 **Input preparation** Consider a pair of datasets $Y \in \mathbb{R}^{N_y \times p_y}$ 624
 567 and $Z \in \mathbb{R}^{N_z \times p_z}$ from two modalities (termed Y -modality 625
 568 and Z -modality for exposition convenience), with each row 626
 569 corresponding to a cell and each column a feature. In the 627
 570 ensuing discussion, we treat Y as the modality with a higher 628
 571 signal-to-noise ratio. For concreteness, one can think of Y 629
 572 as a snRNAseq dataset and Z as a CODEX dataset. Suppose 630
 573 there are two known functions $f_y: \mathbb{R}^{p_y} \rightarrow \mathbb{R}^s$ and $f_z: \mathbb{R}^{p_z} \rightarrow$ 631
 574 \mathbb{R}^s such that $f_y(y)$ predicts the values of $f_z(z)$ in a cell if the 632
 575 measured values under Y -modality are y in that cell and those 633
 576 under Z -modality are z . For any matrix A with p_y columns, 634
 577 let $f_y(A)$ denote the matrix with s columns and the same 635
 578 number of rows as A , obtained from applying f_y on each row 636
 579 of A and stacking the outputs as row vectors. For any matrix 637
 580 B with p_z columns, $f_z(B)$ is analogously defined. With f_y 638
 581 and f_z , we define $Y^\circ = f_y(Y) \in \mathbb{R}^{N_y \times s}$ and $Z^\circ = f_z(Z) \in$ 639
 582 $\mathbb{R}^{N_z \times s}$. In the snRNAseq vs. CODEX example, if one has 640
 583 a crude prediction for a subset S (with size $|S| = s$) of the 641
 584 proteins then $f_z(z) = z_S$ returns the subvector indexed by S 642
 585 while $f_y(y) = \hat{z}_S$ predicts the observed CODEX values for 643
 586 these proteins based on transcriptomic information of a cell. 644
 587 In summary, we start with a pair of original datasets (Y, Z) 645
 588 and a pair of datasets (Y°, Z°) with correspondence of 646
 589 columns based on domain knowledge.

590 **Meta-cell construction** To alleviate sparsity and to scale to 635
 591 large datasets, we start by constructing meta-cells. Take the 636
 592 Y -modality for example. Let n_y be the desired number of 637
 593 meta-cells one aims for. We first construct a nearest-neighbor 638
 594 graph of the rows of Y , apply Leiden clustering with an ap- 639
 595 propriate resolution level to obtain n_y clusters, and average 640

over the rows within each cluster to obtain the features for
 each meta-cell that serves as the representative of the cluster.
 Consequently, we obtain $Y_m \in \mathbb{R}^{n_y \times p_y}$. Using this clustering
 structure (induced by Y as opposed to Y°), we can average
 feature vectors in Y° to obtain $Y_m^\circ \in \mathbb{R}^{n_y \times s}$. When desired,
 the same operation can be performed on the Z -modality to
 obtain $Z_m \in \mathbb{R}^{n_z \times p_z}$ and $Z_m^\circ \in \mathbb{R}^{n_z \times s}$. We recommend only
 constructing meta-cells for modalities with high signal-to-
 ratios. For example, if Y -modality contains snRNAseq data
 and Z -modality contains CODEX data, then we would con-
 struct meta-cells only in Y -modality. After this curation step,
 we have two pairs of datasets (Y_m, Z_m) and (Y_m°, Z_m°) . The for-
 mer pair can have completely distinct feature sets, while the
 latter pair must have matching feature sets with correspond-
 ing columns. In Figure 1A, the former correspond to the pair
 of all feature matrices, and the latter correspond to the pair of
 linked feature matrices.

Fuzzy smoothing Let $G_Y \in \{0, 1\}^{n_y \times n_y}$ be a nearest
 neighbor graph of Y_m where each row i is connected to k_i^Y
 rows that are closest in a chosen similarity measure, includ-
 ing itself. So row i of G_Y has k_i^Y entries equal to one and
 others zeros. In addition, all its diagonal entries are equal to
 one. Let $\mathcal{A}_Y(Y_m) = K_Y^{-1} G_Y Y_m$ and $\mathcal{A}_Y(Y_m^\circ) = K_Y^{-1} G_Y Y_m^\circ$
 be locally averaged versions of Y_m and Y_m° over G_Y , respec-
 tively, where $K_Y = \text{diag}(k_1^Y, \dots, k_{n_y}^Y)$. For a nearest neigh-
 bor graph G_Z , we define $\mathcal{A}_Z(Z_m)$ and $\mathcal{A}_Z(Z_m^\circ)$ in an analo-
 gous way. Finally, for any weight $w \in [0, 1)$ and any matrices
 A and B with n_y and n_z rows respectively, define

$$\begin{aligned} \tilde{A} &= S_Y(A; w) = wA + (1-w)\mathcal{A}_Y(A), \\ \tilde{B} &= S_Z(B; w) = wB + (1-w)\mathcal{A}_Z(B). \end{aligned} \quad (1)$$

In this way, we define $\tilde{Y}_m^\circ = S_Y(Y_m^\circ; w_0)$ and $\tilde{Z}_m^\circ =$
 $S_Z(Z_m^\circ; w_0)$ with $w_0 \in [0, 1)$. In Figure 1A, these are
 the smoothed Y -modality linked features and smoothed Z -
 modality linked features.

Initial matching via linear assignment As the columns in
 \tilde{Y}_m° and in \tilde{Z}_m° have correspondences, we can compute an
 $n_y \times n_z$ distance matrix D° where D_{ij}° measures the distance
 between the i -th row in \tilde{Y}_m° and the j -th row in \tilde{Z}_m° after pro-
 jecting to respective leading singular subspaces. We obtain
 an initial matching $\hat{\Pi}^\circ$ as the solution to the linear assign-
 ment problem (33, 60):

$$\begin{aligned} &\text{minimize} && \langle \Pi, D^\circ \rangle \\ &\text{subject to} && \Pi \in \{0, 1\}^{n_y \times n_z} \\ & && \sum_i \Pi_{ij} \leq 1, \forall j, \quad \sum_j \Pi_{ij} \leq 1, \forall i, \\ & && \sum_{i,j} \Pi_{ij} = n_{\min}. \end{aligned} \quad (2)$$

Here, $n_{\min} = \min\{n_y, n_z\}$ and for two matrices A and B of
 the same size, $\langle A, B \rangle = \sum_{i,j} A_{ij} B_{ij}$ denotes the trace inner
 product. The estimator $\hat{\Pi}^\circ$ provides a relatively crude match-
 ing using only the information provided by the prior knowl-
 edge encapsulated in f_y and f_z that link features in the two
 modalities. By definition, $\hat{\Pi}^\circ$ gives n_{\min} pairs of matched

641 rows between the two modalities. We call these matched 682
642 pairs *initial pivots*. 683

643 Cross-modality joint embedding and iterative refinement of 684 644 matching 685

645 *From matched pairs to joint embedding* An estimated match- 686
646 ing $\hat{\Pi}$ induces a cross-modality joint embedding of Y_m and 687
647 Z_m . In particular, let $Y_m^r \in \mathbb{R}^{n_y \times r_y}$ and $Z_m^r \in \mathbb{R}^{n_z \times r_z}$ collect 688
648 the leading PCs of *all* features (i.e., Y_m and Z_m) in the two 689
649 modalities, respectively. Here, the numbers of PCs to retain, 690
650 i.e., r_y and r_z , are chosen based on data. For any matrix A , let 691
651 $[A]_i$ denote its i -th row. Suppose $\{(i_\ell, i'_\ell) : \ell = 1, \dots, n_{\min}\}$ 692
652 are the matched pairs specified by $\hat{\Pi}$. We perform CCA on 693
653 data pairs 694

$$\{([Y_m^r]_{i_\ell}, [Z_m^r]_{i'_\ell}) : \ell = 1, \dots, n_{\min}\}$$

645 to obtain the leading r_{cc} loading vectors for either modality, 688
646 collected as the columns of $\hat{C}_y = \hat{C}_y(\hat{\Pi})$ and $\hat{C}_z = \hat{C}_z(\hat{\Pi})$, 689
647 respectively. The cross-modal joint embedding induced by 690
648 $\hat{\Pi}$ is then $Y_m^{cc} = Y_m^r \hat{C}_y \in \mathbb{R}^{n_y \times r_{cc}}$ and $Z_m^{cc} = Z_m^r \hat{C}_z \in$ 691
649 $\mathbb{R}^{n_z \times r_{cc}}$, which are the predicted CC scores of Y_m^r and Z_m^r , 692
650 respectively. 693

651 *Iterative refinement* Let $\hat{\Pi}^{(0)} = \hat{\Pi}^\circ$ be the initial matching 688
652 obtained from Eq. (2). Fix a weight $w_1 \in [0, 1)$ and the em- 689
653 bedding dimension r^{cc} , we refine the estimated matching by 690
654 iterating the following steps for $t = 1, \dots, T$: 691

- 655 (i) Compute joint embedding $\{Y_m^{cc,(t)}, Z_m^{cc,(t)}\}$ induced by 688
656 $\hat{\Pi}^{(t-1)}$; 689
- 657 (ii) Apply fuzzy smoothing on joint embedding: $\tilde{Y}_m^{cc,(t)} =$ 690
658 $S_Y(Y_m^{cc,(t)}, w_1)$, $\tilde{Z}_m^{cc,(t)} = S_Z(Z_m^{cc,(t)}, w_1)$; 691
- 659 (iii) Calculate a distance matrix $D^{(t)} \in \mathbb{R}^{n_y \times n_z}$ where $D_{ij}^{(t)}$ 688
660 measures the distance between $[\tilde{Y}_m^{cc,(t)}]_i$ and $[\tilde{Z}_m^{cc,(t)}]_j$, 689
661 and obtain a refined matching $\hat{\Pi}^{(t)}$ by solving Eq. (2) in 690
662 which D° is replaced with $D^{(t)}$. 691

663 Figure 1B illustrates the foregoing refinement iteration. 688

664 **Propagation of matching and post-processing** For down- 688
665 stream analyses, one would often like to find for each cell in 689
666 Y a match in Z when possible, or *vice versa*, and sometimes 690
667 both ways. In addition, we would like to have joint embed- 691
668 ding of cells across different modalities in a common space. 692
669 We now describe how MaxFuse achieves these goals. 693

670 *Filtering and final joint embedding* Upon obtaining the 688
671 matched pairs $\{(i_\ell, i'_\ell) : \ell = 1, \dots, n_{\min}\}$ in $\hat{\Pi}^{(T)}$, we rank 689
672 them in descending order of $D_{i_\ell i'_\ell}^{(T)}$ and only retain the top 690
673 $100 \times (1 - \alpha)\%$ pairs, where α is a user-specified filtering 691
674 proportion (with a default $\alpha = 0$). The retained pairs are 692
675 called *refined pivots*. Then, we fit a CCA using the re- 693
676 fined pivots and the corresponding rows in Y_m and Z_m to 694
677 get the associated CCA loading matrices $\hat{C}_y^e \in \mathbb{R}^{p_y \times r^e}$ and 695
678 $\hat{C}_z^e \in \mathbb{R}^{p_z \times r^e}$. Here the positive integer r^e is a user-specified 696
679 dimension for final joint embedding. Finally, the joint em- 697
680 bedding of the full datasets is given by $Y^e = Y \hat{C}_y^e \in \mathbb{R}^{N_y \times r^e}$ 698
681 and $Z^e = Z \hat{C}_z^e \in \mathbb{R}^{N_z \times r^e}$, respectively. In Figure 1C, they 699

682 correspond to the Y -modality embedding and Z -modality 683
684 embedding matrices. 685

686 *Using pivots to propagate matching* For each row index 687
688 $i \in \{1, \dots, n_y\}$ in Y -modality that does not have a match in 689
689 Z -modality (i.e., i does not belong to any refined pivot), we 690
690 search for the nearest neighbor of the i -th row in \tilde{Y}_m (Y_m after 691
691 fuzzy smoothing) that belongs to some refined pivot. Sup- 692
692 pose the nearest neighbor is the j_i -th row with a match j'_i in 693
693 Z -modality, then we call (i, j'_i) a matched pair obtained via 694
694 *propagation*. We can optionally filter out any matched pair 695
695 via propagation in which the nearest neighbor distance be- 696
696 tween $[\tilde{Y}_m]_i$ and $[\tilde{Y}_m]_{j_i}$ is above a user-specified threshold. 697
697 The retained matched pairs composes the Y -to- Z *propagated* 698
698 *matching*. We then repeat the above procedure with the roles 699
699 of Y - and Z -modalities switched and obtain the Z -to- Y *prop-* 700
700 *agated matching*. 701

702 Pooling all matched pairs from refined pivots and propagated 703
703 matching together, we obtain a matching between meta-cells 704
704 in Y -modality and those in Z -modality. Such a meta-cell 705
705 level matching defines a single-cell level matching between 706
706 the original datasets Y and Z by declaring (i, i') a matched 707
707 pair for $1 \leq i \leq N_y, 1 \leq i' \leq N_z$ if the meta-cell that i belongs 708
708 to is matched to the meta-cell that i' belongs to. 709

710 *Scoring and directional pruning of matching* For each single- 705
711 cell level matched pair (i, i') , we compute Pearson correla- 706
712 tion between the i -th row of Y^e and the i' -th row of Z^e (i.e., 707
713 corresponding rows in final joint embedding) as its matching 708
714 score. We use these matching scores to prune single-cell level 709
715 matching, with the *direction* of pruning specified by user. 710
716 Suppose the user wants to find for each cell in Z a match 711
717 in Y (e.g., Z is a CODEX dataset and Y snRNAseq). Then 712
718 for each cell index $1 \leq i' \leq N_z$, we first list all refined pivots 713
719 and propagated matching pairs that contain i' . If the list is 714
720 non-empty, we only retain the pair with the highest match- 715
721 ing score. Otherwise, we declare no match for cell i' in Z - 716
722 modality. If the direction is reversed, we apply the foregoing 717
723 procedure with the roles of Y and Z switched. Furthermore, 718
724 if no directional pruning is desired, we just keep all refined 719
725 pivots and post-screening propagated matching pairs in the 720
726 final single-cell matching. 721

722 After filtering, propagation, and potential pruning, the final 723
723 list of matched pairs correspond to the final matching in Fig- 724
724 ure 1C. 725

726 **A batched version of MaxFuse.** Single-cell and spatial 727
727 datasets can be large. To facilitate fast computation for large 728
728 datasets, we developed a batched version of MaxFuse. 729

730 **Batching** Fix a desired pair of sample sizes (n_y, n_z) and 731
731 meta-cell ratios $(N_y/n_y, N_z/n_z)$, we randomly partition the 732
732 dataset under Y -modality (resp. Z -modality) into disjoint 733
733 subsets of sizes roughly all equal to N_y (resp. N_z). De- 734
734 note them as $Y^{[1]}, \dots, Y^{[b_y]}$ and $Z^{[1]}, \dots, Z^{[b_z]}$. We then ap- 735
735 ply the MaxFuse pipeline on each pair of data $\{Y^{[l]}, Z^{[m]}\}$, 736
736 $1 \leq l \leq b_y, 1 \leq m \leq b_z$ to get the refined pivots and the *prop-* 737
737 *agated matching*, as well as their induced single-cell level 738
738 matched pairs, for that pair of batches. 739

737 **Stitching** After pooling all refined pivots from all batch
 738 pairs, we obtain a multiple-to-multiple matching. For each
 739 unique cell in Z -modality, we average all its matches in Y -
 740 modality, that is, we average matched cells in the modality
 741 with a higher SNR. After this step, we get a pair of matrices
 742 with rows paired. We then fit CCA on this pair of matrices
 743 and get the loading matrices, which are then used to jointly
 744 embed the whole datasets. Finally, with the joint embedding
 745 of the whole datasets in Y - and Z -modalities, scoring and di-
 746 rectional pruning of matching are performed in the same way
 747 as in MaxFuse without batching.

748 Systematic benchmarks on ground-truth datasets.

749 **MaxFuse and other methods in comparison** MaxFuse was
 750 implemented in Python, and the four methods in comparison,
 751 Seurat V3, Harmony, Liger, and BindSC, were implemented
 752 in R. All benchmarking datasets were preprocessed in the
 753 same way for all methods, including filtering of low-quality
 754 cells, selection of highly variable genes and protein features
 755 to be used in integration, feature linkage scheme (e.g., pro-
 756 tein to their corresponding gene names), and normalization of
 757 raw observed values (except for Liger which required scaling
 758 without centering). We used the default tuning parameters
 759 in each method suggested by the respective tutorial except
 760 for BindSC, for which we used the separate set of param-
 761 eters suggested for the integration of protein-related data by
 762 its method tutorial website. For MaxFuse, initial matching
 763 used features that are weakly linked (e.g., protein CD4 and
 764 RNA *CD4*) and are smoothed by all-feature nearest-neighbor
 765 graphs. For refined matching, all features from both modal-
 766 ities were used (e.g., all proteins and RNAs that are highly
 767 variable). For other methods in comparison, BindSC used
 768 both the weakly linked features and all features, whereas oth-
 769 ers only used the weakly linked features by design. The full
 770 detail (including preprocessing, implementation, and down-
 771 stream analysis and evaluation of MaxFuse and other meth-
 772 ods) is recorded and can be reproduced.

773 Evaluation metrics

- 774 1. Cell type matching accuracy: To evaluate the matching
 775 performance for Seurat, Liger, Harmony, and BindSC, we
 776 used the respective integration embedding vectors pro-
 777 duced by each method. For these methods, for each
 778 cell in one modality, we regarded its nearest neighbor
 779 from the other modality under Pearson correlation dis-
 780 tance in the embedding space as its match. For MaxFuse,
 781 we directly used matched pairs produced in the final re-
 782 sult. For all methods, we use the same matching direc-
 783 tion (e.g., for each cell in CODEX data finding a matched
 784 cell in scRNAseq data) for fair comparison. Accuracy
 785 of the matchings was measured by fraction of matched
 786 pairs with identical cell type annotations. Details on cell
 787 type annotation are given below in the description of each
 788 benchmarking dataset.
- 789 2. FOSCTTM: Fraction of sample closer than true match
 790 (FOSCTTM) was used to evaluate single-cell level align-
 791 ment accuracy on datasets with ground-truth single-cell

level pairing. The measure has been used previously in
 cross-modality alignment benchmarking tasks (19, 36,
 37). For such data, $N_y = N_z = N$, and FOSCTTM is
 defined as:

$$\text{FOSCTTM} = \frac{1}{2N} \left(\sum_{i=1}^N \frac{n_y^{(i)}}{N} + \sum_{i=1}^N \frac{n_z^{(i)}}{N} \right),$$

where for each i , $n_y^{(i)} = |\{j | d(y_i, z_j) < d(y_i, z_i)\}|$ with d
 a distance metric in the joint embedding space and for $l =$
 $1, \dots, N$, y_l and z_l the embedded vectors of the l -th cell
 with its measurements in Y and Z modality, respectively.
 The counts $n_z^{(i)}$, $i = 1, \dots, N$, are defined analogously.
 A lower value of FOSCTTM indicates better integration
 performance.

3. FOSKNN: Fraction of sample with true match among
 k -nearest-neighbors (FOSKNN) was used to evaluate
 single-cell level alignment accuracy on datasets with
 ground-truth single-cell level pairing. For such data,
 $N_y = N_z = N$. For any method in comparison, let
 $\{y_i : i = 1, \dots, N\}$ be the coordinates of cells in the joint
 embedding space from their Y modality information, and
 let $\{z_i : i = 1, \dots, N\}$ be embedding coordiantes from
 their Z modality information. Then

$$\text{FOSKNN} = \frac{1}{2N} \left(\sum_{i=1}^N \mathbf{1}_{E_{y,k}}^{(i)} + \sum_{i=1}^N \mathbf{1}_{E_{z,k}}^{(i)} \right)$$

where for $i = 1, \dots, N$, $\mathbf{1}_{E_{y,k}}^{(i)}$ is the indicator of whether
 the k closest embedded vectors from Z modality to y_i
 includes z_i . The quantity $\mathbf{1}_{E_{z,k}}^{(i)}$ is defined analogously.

4. Silhouette F1 score: Silhouette F1 score has been used
 to simultaneously measure modality mixing and infor-
 mation preservation post-integration process (21, 35).
 In brief, the F1 score was calculated by $2 \cdot \text{slt_mix} \cdot$
 $\text{slt_clust} / (\text{slt_mix} + \text{slt_clust})$, where slt_mix
 is defined as one minus normalized Silhouette width
 with the label being modality index (two modalities);
 slt_clust is defined by the normalized Silhouette width
 with label being cell type annotations (e.g., “CD4 T”,
 “CD8 T”, “B”, etc.). All Silhouette widths were com-
 puted using the `silhouette()` function from R pack-
 age `cluster`.
5. ARI F1 score: Adjusted Random Index F1 score has been
 used to jointly measure modality mixing and information
 preservation post-integration process (21, 35). The score
 was calculated in a similar way to Silhouette F1 score,
 while the Adjusted Random Index was used instead of
 the Silhouette width. All ARI scores were computed us-
 ing the function `adjustedRandIndex()` in R pack-
 age `mclust`.

CITE-seq PBMC dataset The CITE-seq healthy human
 pbmc data with antibody panel of 228 markers was retrieved
 from Hao et al. (34). For benchmarking purposes, 5 batches
 of cells, each with 10k cells were randomly sampled from
 the original dataset, and selected for benchmarking. The first 15

824 components of the embedding vector produced by all meth- 880
825 ods were used for benchmarking metric calculation. The 881
826 UMAP visualization of the integration process was also cal- 882
827 culated with the first 15 components of the embedding vec- 883
828 tors. Cell type annotations (lv1 - 8 cell types and lv2 - 20 884
829 cell types) were directly retrieved from Hao et al.'s original 885
830 annotation. 886

831 For antibody dropping, we ranked the importance of each in- 887
832 dividual antibody in the panel in terms of phenotyping con- 888
833 tribution. The importance score was calculated by training a 889
834 random forest model (function `randomForest` in R pack- 890
835 age `randomForest`, with default parameters) using all an- 891
836 tibodies to predict cell type labels (annotation level 2 from 892
837 Hao et al.), then a permutation feature importance test (func- 893
838 tion `varImp` with default parameters in R package `caret`) 894
839 was performed on the trained model to acquire the individ- 895
840 ual importance scores. Then antibodies were ranked by the 896
841 importance scores, and 4 panels were used for antibody drop- 897
842 ping test: (1) full 228 antibody panel; (2) top 100 most im- 898
843 portant antibodies; (3) top 50 most important antibodies; (4) 899
844 top 30 most important antibodies. 900

845 **CITE-seq BMC dataset** The CITE-seq healthy human 901
846 BMC data with antibody panel of 25 markers was retrieved 902
847 from R package `SeuratData` 'bmcite', originated from Hao 903
848 et al. (34). For benchmarking purpose, a total of 20k cells 904
849 were randomly sampled from the original dataset, and se- 905
850 lected for benchmarking. The first 15 components of the 906
851 embedding vectors produced by all methods were used for 907
852 benchmarking metric calculation. The UMAP visualization 908
853 of the integration process was also calculated with the first 15 909
854 components of the embedding vectors. The original cell type 910
855 annotation (lv2) from the R package was binned into 8 popu- 911
856 lations: "DC", "progenitor", "monocyte", "NK", "B", "CD4 912
857 T", "CD8 T" and "Other T", and used for benchmarking. 913

858 **Ab-seq BMC dataset** The Ab-seq healthy human BMC 914
859 data with antibody panel of 97 markers, and whole transcrip- 915
860 tome sequencing was retrieved from Triana et al. (39). All 916
861 cells in the dataset (~13k), except cells belonging to cell 917
862 types with insufficient amount of cells (< 50 cells, anno- 918
863 tated as "Doublet and Triplets", "Early GMP", "Gamma delta 919
864 T cells", "Immature B cells", "Metaphase MPPs", "Neu- 920
865 trophils" in Triana et al.) were excluded for integration, and 921
866 the remaining 14 cell types were used during benchmarking. 922
867 The first 15 components of the embedding vectors produced 923
868 by all methods were used for benchmarking metric calcula- 924
869 tion. The UMAP visualization of the integration process was 925
870 also calculated with the first 15 components of the embedding 926
871 vectors.

872 **TEA-seq PBMC dataset** The TEA-seq neutrophil-depleted 927
873 human PBMC dataset was retrieved from Swanson et al. 928
874 (41) (GSM4949911). This dataset is stained with 46 929
875 antibodies and contains chromatin accessibility informa- 930
876 tion. Cell type annotation was performed using R package 931
877 `Seurat`(v4) WNN-multi-modal clustering pipeline: func- 932
878 tion `FindMultiModalNeighbors` was run on ADT 933
879 PCA (first 25 components) and ATAC LSI (2-50 com- 934

ponents, calculated by R package `ArchR` (42)). Subse-
quently, function `FindClusters` was used to generate un-
supervised clustering (with parameter `algorithm = 3`,
`resolution = 0.2`), followed by manual annotation. A
total of 8 populations were identified ("Naive CD4", "Mem
CD4", "Monocyte", "NK", "Naive CD8", "Mem CD8", "Ef-
fector CD8", "B", "NK"), and the total amount of cells was
~7.4k. ADT expressions and gene activity scores (calculated
by R package `ArchR` (42)) were used as input for Max-
Fuse and other methods. Additionally, during matching re-
finement, MaxFuse used LSI reduction of the ATAC peaks
(first 2-50 components) as features for the ATAC modality.
The first 15 components of the embedding vectors produced
by all methods were used for benchmarking metric calcula-
tion. The UMAP visualization of the integration process was
also calculated with the first 15 components of the embedding
vectors.

ASAP-seq PBMC dataset The ASAP-seq healthy human
PBMC data (CD28 & CD3 stim PBMC control group) with
an antibody panel of 227 markers, and chromatin accessi-
bility information was retrieved from Mimitou et al. (40)
(GSM4732109). Cell type annotation was performed using
R package `Seurat`(v4) WNN-multi-modal clustering
pipeline: function `FindMultiModalNeighbors` was
run on ADT PCA (first 18 components) and ATAC LSI (2-
40 components, calculated by R package `ArchR`). Subse-
quently, function `FindClusters` was used to generate un-
supervised clustering (with parameter `algorithm = 3`,
`resolution = 0.3`), followed by manual annotation. A
total of 9 populations were identified ("Naive CD4", "Mem
CD4", "Monocyte", "NK", "Naive CD8", "Mem CD8", "B",
"OtherT", "dirt"), and "dirt" was removed from subsequent
usage, resulting in ~4.4 k cells used. ADT expressions and
gene activity scores (calculated by R package `ArchR`) were
used as input for MaxFuse and other methods. Additionally,
during matching refinement, MaxFuse used LSI reduction of
the ATAC peaks (First 2-50 components) as features for the
ATAC modality. The first 15 components of the embedding
vectors produced by all methods were used for benchmarking
metric calculation. The UMAP visualization of the integra-
tion process was also calculated with the first 15 components
of the embedding vectors.

MaxFuse on Spatial-omics matching.

CODEX and scRNA-seq human tonsil CODEX multi-
plexed imaging data of human tonsil tissues with a panel of
46 antibodies were retrieved from Kennedy-Darling et al.
(47). Images from tonsil-9338 (region X2-8, Y7-15) were
used. Whole-cell segmentation was performed with a local
implementation of Mesmer (61), with weights downloaded
from: https://deepcell-data.s3-us-west-1.amazonaws.com/model-weights/Multiplex_Segmentation_20200908_2_head.h5. Inputs of
segmentation were DAPI (nuclear) and CD45 (membrane).
Signals from the images were capped at 99.7th percentile,
with prediction parameter `model_mpp = 0.8`. Cells

smaller than 30 pixels or larger than 800 pixels were excluded. Signals from individual cells were then extracted and scaled to the [0,1] interval, with percentile cutoffs of 0.5% (floor) and 99.5% (ceiling). Cell type annotation was performed using R package *Seurat* clustering pipeline: function `FindNeighbors` was run on CODEX protein PCA (first 15 components). Subsequently, function `FindClusters` was used to generate unsupervised clustering (with parameter `resolution = 1`), followed by manual annotation. A total of 9 populations were identified (“B-CD22-CD40”, “B-Ki67”, “Plasma”, “CD4 T”, “CD8 T”, “DC”, “Fibro/Epi”, “Vessel”, “Other”, and “Dirt”), and 6 populations (~180k cells) were used in subsequent analysis (“B-CD22-CD40”, “B-Ki67”, “Plasma”, “CD4 T”, “CD8 T”, and “DC”).

Single-cell RNA-seq data of dissociated human tonsil cells were retrieved from King et al. (48). The pre-processing and cell typing steps were done in R package *Seurat*, following the description presented in King et al. In brief, tonsil cells (“t1”, “t2” and “t3”) were merged, then filtered by criteria: `nFeature_RNA > 200 & nFeature_RNA < 7500 & percent.mt < 20`, and subsequently value normalized by function `SCTransform`. Harmony batch correction was performed for different tonsils, with function `RunHarmony`. Unsupervised clustering was performed by function `FindNeighbors` with harmony embedding (1-27 dimensions) and function `FindClusters` with `resolution = 0.5`. A total of 8 populations was defined (“B-CD22-CD40”, “B-Ki67”, “circulating B”, “Plasma”, “CD4 T”, “CD8 T”, “DC”, “Other”), and 6 populations (~13k cells) were used in subsequent analysis (“B-CD22-CD40”, “B-Ki67”, “Plasma”, “CD4 T”, “CD8 T”, and “DC”).

Boundaries of germinal centers from the CODEX images were drawn manually, and dilation and erosion from the boundary was performed with python package *skimage*, with function `morphology.binary_dilation` and `morphology.disk`. Ten layers inward or outward from the boundary (each layer = 30 pixels, resolution: 376nm/pixel) was performed. Cells were assigned to each layer by their centroids’ locations. The RNA expression level from each layer, based on the averaged CODEX matched scRNA-seq cells, were plotted with R package *ggplot2*. The UMAP visualization of the integration process was calculated with the first 15 components of the embedding vectors.

HUBMAP atlas: CODEX, snRNA-seq and snATAC-seq human intestine CODEX multiplex imaging (48 markers), snRNA-seq and snATAC-seq of healthy human intestine cells were acquired from Hickey et al. (32). For CODEX, samples “B005_SB” and “B006_CL” were used, while for snRNA-seq and snATAC-seq, single-ome sequencing data of four donors (“B001”, “B004”, “B005”, “B006”) from the study were used. Cells annotated as “B cells”, “T cells”, “Endothelial”, “Enteroendocrine”, “Goblet”, “Mono_Macrophages”, “Plasma”, “Smooth muscle”, and “Stroma” were selected for the integration process. Cell counts for each modality

used for MaxFuse were: CODEX ~100k (small bowel) and ~70k (colon); snRNA-seq ~32k (small bowel) and ~16k (colon); snATAC-seq ~28k (small bowel) and ~21k (colon). CODEX protein expressions, snRNA-seq RNA expressions, snATAC-seq gene activity scores and LSI scores (calculated with R package *ArchR*) were used as MaxFuse input (RNA expressions, gene activity scores and LSI scores were batch-corrected by Harmony (20), based on patient ID). The matching and integration process was done on colon and small bowel samples respectively.

Pairwise MaxFuse alignments of cells between protein (CODEX) and RNA (snRNA-seq), and cells between RNA (snRNA-seq) and ATAC (snATAC-seq) were performed. Refined pivots from the two bi-modal alignments were chained together by using the pivot cells in the RNA modality as the intermediary, resulting in a list of tri-modal pivots linking all three modalities. Subsequently, we used these pivots to calculate a tri-omic embedding via generalized CCA (*gccca*) (21, 55). In particular, we used the *gccca* formulation and algorithm described in (21).

The UMAP visualization of the tri-modal integration was calculated with the first 15 components of the embedding vectors (*gccca* scores in this case). Embeddings of CODEX cells were overlaid with their protein expressions, or their matched cells’ RNA expressions, or gene activity scores. Spatial locations of these expression values and scores were plotted based on CODEX cells’ x-y centroid locations. Additionally, we showed spatial locations of transcription factor motif enrichment scores (Z-score) of CODEX cells, based on their matched snRNA-seq cells, which were calculated by R package *chromVAR* (56). All values were capped between 5%–95% quantiles for visualization purpose during plotting.

Benchmark on ground-truth strongly linked modalities.

MaxFuse and other methods specialized in ATAC-RNA integration in comparison We compared MaxFuse to three methods that specialize in ATAC-RNA integration: *scGLUE* (19), *Maestro* (62) and *scJoint* (63). For MaxFuse, the initial matching used the gene activity scores, while during refined matching the active RNA features and LSI embedding from ATAC were used. For other methods in comparison, we used their default settings. Metrics used for benchmarking were calculated similarly as described in previous sections. The full detail (including preprocessing, implementation, and downstream analysis and evaluation of MaxFuse and other methods specialized in ATAC-RNA integration) is recorded and can be reproduced.

Multioome scRNA - scATAC-seq human retina dataset Multioome (scRNA-seq & scATAC-seq) data of human retina cells was retrieved from Wang et al. (46). For input required by MaxFuse: gene activity and LSI scores of ATAC cells were calculated by R package *ArchR* using the fragment files, while RNA counts were directly extracted. For other methods in comparison, we used their default settings. For benchmarking, a total of 20k cells were randomly sampled

1047 and used for testing. All cell types were used during integra-1109
1048 tion (“Rod”, “OFF cone bipolar”, “Mullerglia”, “ON cone
1049 bipolar”, “Rod bipolar”, “Cone”, “GABA amacrine”, “Hor-1110
1050 izontal”, “Glyamacrine”, “AII amacrine”, “Retinal ganglion1111
1051 cell”, “Astrocyte”, “Microglia”, annotated by Wang et al.).1112
1052 The first 15 components of the embedding vectors produced1113
1053 by all methods were used for benchmarking metric calcula-1114
1054 tion.1115

1055 **10x Multiome peripheral blood mononuclear cells** Multi-1121
1056 ome (scRNA-seq & scATAC-seq) data of human mononu-1122
1057 clear peripheral blood cells was retrieved from the 10x pub-1123
1058 lic data repository (44). For input required by MaxFuse: gene1124
1059 activity and LSI scores of ATAC modality were calculated by1125
1060 R package *Signac*, the latter using the fragment files. RNA1126
1061 counts were directly extracted from the *cellranger* out-1127
1062 put. Cell-type labels were transferred from CITE-seq PBMC1128
1063 reference (34) using the method in (34).1129

1064 **10x Multiome day 18 embryonic mouse brain cells** Multi-1135
1065 ome (scRNA-seq & scATAC-seq) data of developing mouse1136
1066 brain cells was retrieved from the 10x public data reposi-1137
1067 tory (44). For input required by MaxFuse: gene activity and1138
1068 LSI scores of ATAC modality were calculated by R package1139
1069 *Signac*, the latter using the fragment files. RNA counts1140
1070 were directly extracted from the *cellranger* output. Cell-1141
1071 type labels were transferred from (64) using the method in1142
1072 (65).1143

1073 **10x Multiome developing human cerebral cortex cells** Multi-1150
1074 ome (scRNA-seq & scATAC-seq) data of developing1151
1075 human cerebral cortex cells was retrieved from Trevino et1152
1076 al. (45). For input required by MaxFuse: gene activity and1153
1077 LSI scores of ATAC modality were calculated by R package1154
1078 *Signac* using the fragment files. RNA counts and ATAC1155
1079 peak matrices were extracted from 10x *cellranger* out-1156
1080 put. The cell-type labels were taken from the original publi-1157
1081 cation.1158

1082 ACKNOWLEDGEMENTS

1083 We thank Yuchao Jiang for initial discussions and for sharing the pre-processed1166
1084 data for 10x multiome PBMC and embryonic mouse brain datasets. B.Z. is sup-1167
1085 ported by a Stanford Graduate Fellowship. This work was funded in part by1168
1086 grants from the National Science Foundation DMS-2210104 (Z.M.), the National1169
1087 Institutes of Health R01-HG006137-11, U2C-CA233285 (N.R.Z.), Mark Foundation1170
1088 Center for Radiobiology and Immunology (N.R.Z.), the US Food and Drug Admin-1171
1089 istration Medical Countermeasures Initiative contracts HHSF223201610018C and1172
1090 75F40120C00176 (G.P.N.), the Parker Institute for Cancer Immunotherapy (G.P.N.),1173
1091 and the Rachford and Carlota A. Harris Endowed Professorship (G.P.N.). This ar-1174
1092 ticle reflects the views of the authors and should not be construed as representing1175
1093 the views or policies of the NSF, FDA, NIH, BMGF, Botnar Foundation or other insti-1176
1094 tutions who provided funding.1177

1095 AUTHOR CONTRIBUTIONS

1096 Conceptualization: S.C., B.Z., G.P.N., N.R.Z., Z.M.1179
1097 Algorithm Development and Implementation: S.C., N.R.Z., Z.M.1180
1098 Analysis: S.C., B.Z., S.H., Z.M.1181
1099 Contribution of Key Reagents and Tools: J.W.H., K.Z.L., M.S., W.J.G, G.P.N.1182
1100 Supervision: G.P.N., N.R.Z., Z.M.1183
11011184

1102 Both S.C. and B.Z. contributed equally and have the right to list their name first in1186
1103 their CV.1187

1104 CONFLICT OF INTERESTS

1105 G.P.N. received research grants from Pfizer, Inc.; Vaxart, Inc.; Celgene, Inc.; and1189
1106 Juno Therapeutics, Inc. during the course of this work. G.P.N. and Y.G. have equity1190
1107 in Akoya Biosciences, Inc. G.P.N. is a scientific advisory board member of Akoya1191
1108 Biosciences, Inc.1192

Reference

1. Marlon Stoeckius, Christoph Hafemeister, William Stephenson, Brian Houck-Loomis, Pratik K Chattopadhyay, Harold Swerdlow, Rahul Satija, and Peter Smibert. Simultaneous epitope and transcriptome measurement in single cells. *Nature methods*, 14(9):865–868, 2017.
2. Payam Shahi, Samuel C Kim, John R Haliburton, Zev J Gartner, and Adam R Abate. Ab-seq: Ultrahigh-throughput single cell protein profiling with droplet microfluidic barcoding. *Scientific reports*, 7(1):1–12, 2017.
3. Dominic Grün and Alexander van Oudenaarden. Design and analysis of single-cell sequencing experiments. *Cell*, 163(4):799–810, 2015.
4. Ino D Karemaker and Michiel Vermeulen. Single-cell dna methylation profiling: technologies and biological applications. *Trends in biotechnology*, 36(9):952–965, 2018.
5. Marek Bartosovic, Mukund Kabbe, and Gonçalo Castelo-Branco. Single-cell cut&tag profiles histone modifications and transcription factors in complex tissues. *Nature biotechnology*, 39(7):825–835, 2021.
6. Sebastian Preissl, Kyle J Gaulton, and Bing Ren. Characterizing cis-regulatory elements using single-cell epigenomics. *Nature Reviews Genetics*, pages 1–23, 2022.
7. Wai Lim Ku, Kosuke Nakamura, Weiwei Gao, Kairong Cui, Gangqing Hu, Qingsong Tang, Bing Ni, and Keji Zhao. Single-cell chromatin immunocleavage sequencing (scchic-seq) to profile histone modification. *Nature methods*, 16(4):323–325, 2019.
8. Caleb A Lareau, Fabiana M Duarte, Jennifer G Chew, Vinay K Kartha, Zach D Burkett, Andrew S Kohlway, Dmitry Pokholok, Martin J Aryee, Frank J Steemers, Ronald Lebofsky, et al. Droplet-based combinatorial indexing for massive-scale single-cell chromatin accessibility. *Nature Biotechnology*, 37(8):916–924, 2019.
9. Anjali Rao, Dalia Barkley, Gustavo S França, and Itai Yanai. Exploring tissue architecture using spatial transcriptomics. *Nature*, 596(7871):211–220, 2021.
10. Yury Goltsev, Nikolay Samusik, Julia Kennedy-Darling, Salil Bhatta, Matthew Hale, Gustavo Vazquez, Sarah Black, and Garry P Nolan. Deep profiling of mouse splenic architecture with codex multiplexed imaging. *Cell*, 174(4):968–981, 2018.
11. Michael Angelo, Sean C Bendall, Rachel Finck, Matthew B Hale, Chuck Hitzman, Alexander D Borowsky, Richard M Levenson, John B Lowe, Scot D Liu, Shuchun Zhao, et al. Multiplexed ion beam imaging of human breast tumors. *Nature medicine*, 20(4):436–442, 2014.
12. Charlotte Giesen, Hao AO Wang, Denis Schapiro, Nevena Zivanovic, Andrea Jacobs, Bodo Hattendorf, Peter J Schüffler, Daniel Grolimund, Joachim M Buhmann, Simone Brandt, et al. Highly multiplexed imaging of tumor tissues with subcellular resolution by mass cytometry. *Nature methods*, 11(4):417–422, 2014.
13. Shanshan He, Ruchir Bhatt, Carl Brown, Emily A Brown, Derek L Buhr, Kan Chantranuvatana, Patrick Danaher, Dwayne Dunaway, Ryan G Garrison, Gary Geiss, et al. High-plex imaging of rna and proteins at subcellular resolution in fixed tissue by spatial molecular imaging. *Nature Biotechnology*, pages 1–13, 2022.
14. Emma Lundberg and Georg HH Börner. Spatial proteomics: a powerful discovery tool for cell biology. *Nature Reviews Molecular Cell Biology*, 20(5):285–302, 2019.
15. Yanxiang Deng, Marek Bartosovic, Sai Ma, Di Zhang, Petra Kukanja, Yang Xiao, Graham Su, Yang Liu, Xiaoyu Qin, Gorazd B Rosoklija, et al. Spatial profiling of chromatin accessibility in mouse and human tissues. *Nature*, 609(7926):375–383, 2022.
16. Ricard Argelaguet, Anna SE Cuomo, Oliver Stegle, and John C Marioni. Computational principles and challenges in single-cell data integration. *Nature biotechnology*, 39(10):1202–1215, 2021.
17. Yang Xu and Rachel Patton McCord. Diagonal integration of multimodal single-cell data: potential pitfalls and paths forward. *Nature Communications*, 13(1):1–4, 2022.
18. Jinzhuang Dou, Shaoheng Liang, Vakul Mohanty, Xuesen Cheng, Sangbae Kim, Jongsu Choi, Yumei Li, Katayoun Rezvani, Rui Chen, and Ken Chen. Unbiased integration of single cell multi-omics data. *BioRxiv*, 2020.
19. Zhi-Jie Cao and Ge Gao. Multi-omics single-cell data integration and regulatory inference with graph-linked embedding. *Nature Biotechnology*, pages 1–9, 2022.
20. Ilya Korsunsky, Nghia Millard, Jean Fan, Kamil Slowikowski, Fan Zhang, Kevin Wei, Yuriy Baglaenko, Michael Brenner, Po-ru Loh, and Soumya Raychaudhuri. Fast, sensitive and accurate integration of single-cell data with harmony. *Nature methods*, 16(12):1289–1296, 2019.
21. Bokai Zhu, Shuxiao Chen, Yunhao Bai, Han Chen, Nilanjan Mukherjee, Gustavo Vazquez, David R McIlwain, Alexander Tzankov, Ivan T Lee, Matthias S Maller, et al. Robust single-cell matching and multi-modal analysis using shared and distinct features reveals orchestrated immune responses. *bioRxiv*, 2021.
22. Joshua D Welch, Velina Kozareva, Ashley Ferreira, Charles Vanderburg, Carly Martin, and Evan Z Macosko. Single-cell multi-omic integration compares and contrasts features of brain cell identity. *Cell*, 177(7):1873–1887, 2019.
23. Kevin E Wu, Kathryn E Yost, Howard Y Chang, and James Zou. Babel enables cross-modality translation between multiomic profiles at single-cell resolution. *Proceedings of the National Academy of Sciences*, 118(15):e2023070118, 2021.
24. Tim Stuart, Andrew Butler, Paul Hoffman, Christoph Hafemeister, Eithymia Papalexi, William M Mauck III, Yuhan Hao, Marlon Stoeckius, Peter Smibert, and Rahul Satija. Comprehensive integration of single-cell data. *Cell*, 177(7):1888–1902, 2019.
25. Zhen Miao, Benjamin D Humphreys, Andrew P McMahon, and Junhyong Kim. Multi-omics integration in the age of million single-cell data. *Nature Reviews Nephrology*, 17(11):710–724, 2021.
26. Jinzhuang Dou, Shaoheng Liang, Vakul Mohanty, Qi Miao, Yuefan Huang, Qingnan Liang, Xuesen Cheng, Sangbae Kim, Jongsu Choi, Yumei Li, et al. Bi-order multimodal integration of single-cell data. *Genome biology*, 23(1):1–25, 2022.
27. Zhana Duren, Xi Chen, Mahdi Zamanighomi, Wanwen Zeng, Ansuman T Satpathy, Howard Y Chang, Yong Wang, and Wing Hung Wong. Integrative analysis of single-cell genomics data by coupled nonnegative matrix factorizations. *Proceedings of the National Academy of Sciences*, 115(30):7723–7728, 2018.
28. Vivien Marx. A dream of single-cell proteomics. *Nature Methods*, 16(9):809–812, 2019.
29. Vidhya M. Ravi, Paulina Will, Jan Kueckelhaus, Na Sun, Kevin Joseph, Henrike Salié, Lea

- 1194 Vollmer, Ugne Kuliesiute, Jasmin von Ehr, Jasim K. Benotmane, Nicolas Neidert, Mariet280
1195 Follo, Florian Scherer, Jonathan M. Goeldner, Simon P. Behringer, Pamela Franco, Mo-1281
1196 hamed Khat, Junyi Zhang, Ulrich G. Hofmann, Christian Fung, Franz L. Ricklefs, Ka-1282
1197 trin Lamszus, Melanie Boerries, Manching Ku, Jürgen Beck, Roman Sankowski, Marius283
1198 Schwabenland, Marco Prinz, Ulrich Schüller, Saskia Killmer, Bertram Bengsch, Axel K.1284
1199 Walch, Daniel Delev, Oliver Schnell, and Dieter Henrik Heiland. Spatially resolved multi-1285
1200 omics deciphers bidirectional tumor-host interdependence in glioblastoma. *Cancer Cell*, 40:1286
1201 (6):639–655.e13, 2022. ISSN 1535-6108. doi: <https://doi.org/10.1016/j.ccell.2022.05.009>. 1287
1202 30. Amin Abedini, Ziyuan Ma, Julia Frederick, Poonam Dhillon, Michael S Balzer, Rojesh288
1203 Shrestha, Hongbo Liu, Steven Vitale, Kishor Devalaraja-Narashimha, Paola Grandi, et al.1289
1204 Spatially resolved human kidney multi-omics single cell atlas highlights the key role of the290
1205 fibrotic microenvironment in kidney disease progression. *bioRxiv*, 2022. 1291
1206 31. Anuja Sathé, Kaishu Mason, Susan M Grimes, Zilu Zhou, Billy T Lau, Xiangqi Bai, Andrew292
1207 Su, Xiao Tan, H Lee, Carlos J Suarez, et al. Colorectal cancer metastases in the liver estab-293
1208 lish immunosuppressive spatial networking between tumor associated sp1+ macrophages294
1209 and fibroblasts. *Clinical Cancer Research: An Official Journal of the American Association*295
1210 *for Cancer Research*, pages CCR–22, 2022. 1296
1211 32. John W Hickey, Winston R Becker, Stephanie A Nevins, Aaron Horning, Almudena Espint297
1212 Perez, Roxanne Chiu, Derek C Chen, Daniel Cotter, Edward D Esplin, Annika K Weimer,298
1213 et al. High resolution single cell maps reveals distinct cell organization and function across299
1214 different regions of the human intestine. *bioRxiv*, 2021. 1300
1215 33. Rainer Burkard, Mauro Dell'Amico, and Silvano Martello. *Assignment problems: revised*301
1216 *reprint*. SIAM, 2012. 1302
1217 34. Yuhao Hao, Stephanie Hao, Erica Andersen-Nissen, William M Mauck III, Shiwei Zheng,1303
1218 Andrew Butler, Maddie J Lee, Aaron J Wilk, Charlotte Darby, Michael Zager, et al. Integrated304
1219 analysis of multimodal single-cell data. *Cell*, 184(13):3573–3587, 2021. 1305
1220 35. Hoa Thi Nhu Tran, Kok Siang Ang, Marion Chevrier, Xiaomeng Zhang, Nicole Yee Shint306
1221 Lee, Michelle Goh, and Jimmiao Chen. A benchmark of batch-effect correction methods for307
1222 single-cell rna sequencing data. *Genome biology*, 21(1):1–32, 2020. 1308
1223 36. Jie Liu, Yuanhao Huang, Ritambhara Singh, Jean-Philippe Vert, and William Stafford Noble.1309
1224 Jointly embedding multiple single-cell omics measurements. In *Algorithms in bioinforma*1310
1225 *ics... International Workshop, WABI... proceedings. WABI (Workshop)*, volume 143. NIH:311
1226 Public Access, 2019. 1312
1227 37. April R Kriebel and Joshua D Welch. Uinmf performs mosaic integration of single-cell multi-1313
1228 omic datasets using nonnegative matrix factorization. *Nature communications*, 13(1):1–17,1314
1229 2022. 1315
1230 38. Etienne Becht, Leland McInnes, John Healy, Charles-Antoine Dutertre, Immanuel WH1316
1231 Kwok, Lai Guan Ng, Florent Ginhoux, and Evan W Newell. Dimensionality reduction for1317
1232 visualizing single-cell data using umap. *Nature biotechnology*, 37(1):38–44, 2019. 1318
1233 39. Sergio Triana, Dominik Vonficht, Lea Jopp-Saile, Simon Raffel, Raphael Lutz, Daniel319
1234 Leonce, Magdalena Antas, Pablo Hernández-Malmierca, Diana Ordoñez-Rueda, Beáta Ra-1320
1235 masz, et al. Single-cell proteo-genomic reference maps of the hematopoietic system enable1321
1236 the purification and massive profiling of precisely defined cell states. *Nature immunology*,1322
1237 22(12):1577–1589, 2021. 1323
1238 40. Eleni P Mimitou, Caleb A Lareau, Kelvin Y Chen, Andre L Zorzetto-Fernandes, Yuhao Hao,
1239 Yusuke Takeshima, Wendy Luo, Tse-Shun Huang, Bertrand Z Yeung, Ethymia Papalex, et al.
1240 Scalable, multimodal profiling of chromatin accessibility, gene expression and protein
1241 levels in single cells. *Nature biotechnology*, 39(10):1246–1258, 2021. 1318
1242 41. Elliott Swanson, Cara Lord, Julian Reading, Alexander T Heubeck, Palak C Genge, Zachary
1243 Thomson, Morgan DA Weiss, Xiao-jun Li, Adam K Savage, Richard R Green, et al. Simulta-
1244 neous trimodal single-cell measurement of transcripts, epitopes, and chromatin accessibility
1245 using tea-seq. *Elife*, 10:e63632, 2021. 1319
1246 42. Jeffrey M Granja, M Ryan Corcos, Sarah E Pierce, S Tansu Bagdatli, Hani Choudhry,
1247 Howard Y Chang, and William J Greenleaf. Archr is a scalable software package for inte-
1248 grative single-cell chromatin accessibility analysis. *Nature genetics*, 53(3):403–411, 2021. 1320
1249 43. Kevin Z. Lin and Nancy R. Zhang. Quantifying common and distinct information in single-cell
1250 multimodal data with tilted-cca. *bioRxiv*, 2022. doi: 10.1101/2022.10.07.511320. 1321
1251 44. 10X Genomics. 10x genomics datasets, 2022. 1322
1252 45. Alexandro E Trevino, Fabian Müller, Jimena Andersen, Lakshman Sundaram, Arwa
1253 Kathiria, Anna Shcherbina, Kyle Farh, Howard Y Chang, Anca M Paşca, Anshul Kundaje,
1254 et al. Chromatin and gene-regulatory dynamics of the developing human cerebral cortex at
1255 single-cell resolution. *Cell*, 184(19):5053–5069, 2021. 1323
1256 46. Sean K Wang, Surag Nair, Rui Li, Katerina Kraft, Anusri Pampari, Aman Patel, Joyce B
1257 Kang, Christy Luong, Anshul Kundaje, and Howard Y Chang. Single-cell multiome of the
1258 human retina and deep learning nominate causal variants in complex eye diseases. *bioRxiv*,
1259 2022. 1324
1260 47. Julia Kennedy-Darling, Salil S Bhaté, John W Hickey, Sarah Black, Graham L Barlow,
1261 Gustavo Vazquez, Vishal G Venkatarraaman, Nikolay Samusik, Yury Goltsev, Christian M
1262 Schürch, et al. Highly multiplexed tissue imaging using repeated oligonucleotide exchange
1263 reaction. *European Journal of Immunology*, 51(5):1262–1277, 2021. 1325
1264 48. Hamish W King, Kristen L Wells, Zohar Shipony, Arwa S Kathiria, Lisa E Wagar, Caleb
1265 Lareau, Nara Orban, Robson Capasso, Mark M Davis, Lars M Steinmetz, et al. Integrated
1266 single-cell transcriptomics and epigenomics reveals strong germinal center-associated eti-
1267 ology of autoimmune risk loci. *Science Immunology*, 6(64):eabh3768, 2021. 1326
1268 49. Stella Maris Ranuncolo, Jose M Polo, Jamil Dierov, Michael Singer, Tracy Kuo, John Grealley,
1269 Roland Green, Martin Carroll, and Ari Melnick. Bcl-6 mediates the germinal center b cell
1270 phenotype and lymphomagenesis through transcriptional repression of the dna-damage
1271 sensor atr. *Nature immunology*, 8(7):705–714, 2007. 1327
1272 50. Masayuki Kuraoka, T Matt Holl, Dongmei Liao, Mandy Womble, Derek W Cain, Alexander E
1273 Reynolds, and Garnett Kelsøe. Activation-induced cytidine deaminase mediates central
1274 tolerance in b cells. *Proceedings of the National Academy of Sciences*, 108(28):11560–
1275 11565, 2011. 1328
1276 51. Antony B Holmes, Clarissa Corinaldesi, Qiong Shen, Rahul Kumar, Nicolo Compagno,
1277 Zhong Wang, Mor Nitzan, Eli Grunstein, Laura Pasqualucci, Riccardo Dalla-Favera, et al.
1278 Single-cell analysis of germinal-center b cells informs on lymphoma cell of origin and out-
1279 come. *Journal of Experimental Medicine*, 217(10), 2020. 1329
52. Dan Suan, Nike J Kräutler, Jesper LV Maag, Danyal Butt, Katherine Bourne, Jana R Her-
mes, Danielle T Avery, Clara Young, Aaron Statham, Michael Elliott, et al. Ccr6 defines
memory b cell precursors in mouse and human germinal centers, revealing light-zone loca-
tion and predominant low antigen affinity. *Immunity*, 47(6):1142–1153, 2017. 1330
53. Sean P Saunders, Erica GM Ma, Carlos J Aranda, and Maria A Curotto de Lafaille. Non-
classical b cell memory of allergic ige responses. *Frontiers in immunology*, 10:715, 2019. 1331
54. Lyssia Belarif, Caroline Mary, Lola Jacquemont, Hoa Le Mai, Richard Danger, Jeremy Her-
vouet, David Minault, Virginie Thepenier, Veronique Nerrière-Daguin, Elisabeth Nguyen,
et al. Il-7 receptor blockade blunts antigen-specific memory t cell responses and chronic
inflammation in primates. *Nature communications*, 9(1):1–13, 2018. 1332
55. Jon R Kettenring. Canonical analysis of several sets of variables. *Biometrika*, 58(3):433–
451, 1971. 1333
56. Alicia N Schep, Beijing Wu, Jason D Buenrostro, and William J Greenleaf. chromVAR: in-
ferring transcription-factor-associated accessibility from single-cell epigenomic data. *Nature
methods*, 14(10):975–978, 2017. 1334
57. Sorim Nam and Jong-Seok Lim. Essential role of interferon regulatory factor 4 (irf4) in
immune cell development. *Archives of pharmacal research*, 39(11):1548–1555, 2016. 1335
58. Jonathan P Katz, Nathalie Perreault, Bree G Goldstein, Catherine S Lee, Patricia A Labosky,
Vincent W Yang, and Klaus H Kaestner. The zinc-finger transcription factor klf4 is required
for terminal differentiation of goblet cells in the colon. 2002. 1336
59. Zhigao Wang, Da-Zhi Wang, GC Teg Pipes, and Eric N Olson. Myocardin is a master
regulator of smooth muscle gene expression. *Proceedings of the National Academy of
Sciences*, 100(12):7129–7134, 2003. 1337
60. Shuxiao Chen, Sizun Jiang, Zongming Ma, Garry P Nolan, and Bokai Zhu. One-way match-
ing of datasets with low rank signals. *arXiv preprint arXiv:2204.13858*, 2022. 1338
61. Noah F Greenwald, Geneva Miller, Erick Moen, Alex Kong, Adam Kagel, Thomas
Dougherty, Christine Camacho Fullaway, Brianna J McIntosh, Ke Xuan Leow, Morgan Sarah
Schwartz, et al. Whole-cell segmentation of tissue images with human-level performance
using large-scale data annotation and deep learning. *Nature biotechnology*, 40(4):555–565,
2022. 1339
62. Chenfei Wang, Dongqing Sun, Xin Huang, Changxin Wan, Ziyi Li, Ya Han, Qian Qin, Jingyu
Fan, Xintao Qiu, Yingtian Xie, et al. Integrative analyses of single-cell transcriptome and
regulome using maestro. *Genome biology*, 21(1):1–28, 2020. 1340
63. Yingxin Lin, Tung-Yu Wu, Sheng Wan, Jean YH Yang, Wing H Wong, and YX Wang. scjoint
integrates atlas-scale single-cell rna-seq and atac-seq data with transfer learning. *Nature
Biotechnology*, 40(5):703–710, 2022. 1341
64. Gioele La Manno, Kimberly Siletti, Alessandro Furlan, Daniel Gyllborg, Elin Vinsland, Ale-
jandro Mossi Albiach, Christoffer Mattsson Langseth, Irina Khven, Alex R Lederer, Lisa M
Dratva, et al. Molecular architecture of the developing mouse brain. *Nature*, 596(7870):
92–96, 2021. 1342
65. Mo Huang, Zhaojun Zhang, and Nancy R Zhang. Dimension reduction and denoising of
single-cell rna sequencing data in the presence of observed confounding variables. *bioRxiv*,
2020. 1343